minerals

MDPI

Article

Fluid Evolution and Controls on Gold Precipitation at the Dongga Au Deposit, Tibet, China: Insights from Pyrite Trace Elements

Hongyu Zhan [1], Qing He [2,*], Yulin Deng [1,*], Chen Li [1], Zuopeng Xiang [1], Changyi Wu [1], Kai Jiang [3] and Xinghai Lang [1]

[1] College of Earth and Planetary Sciences, Chengdu University of Technology, Chengdu 610059, China; m13990526329@163.com (H.Z.); 15548443121@163.com (C.L.); x_ly666@163.com (Z.X.); wuchangyi0001@163.com (C.W.); langxinghai@126.com (X.L.)
[2] Western Mining Group Co., Ltd., Xining 810003, China
[3] Tibet Tianyuan Mineral Exploration Co., Ltd., Xigaze 857000, China; wangyiyj2021@163.com
* Correspondence: heqing7274@163.com (Q.H.); dengyulin@cdut.edu.cn (Y.D.)

Abstract

The Dongga Au deposit is located in the giant Xiongcun porphyry Cu-Au ore district within the Southern Lhasa terrane; however, the evolution of ore-forming fluids and the mechanisms of gold precipitation during the main mineralization stage remain poorly constrained. This study integrates geological observations and in situ LA-ICP-MS trace element analyses of pyrite to address the above issues. Three generations of pyrite are identified: Py1 occurring in quartz–sulfide veins, Py2 in chlorite–sulfide veins, and Py3 in pyrite veins. Trace element data show that Au and As contents are relatively low in all three pyrite generations and mainly occur as lattice-bound elements, whereas Pb, Ag, Bi, Cu, and Zn are predominantly hosted in micro- to nano-scale mineral inclusions. Ore-forming temperatures estimated from Se concentrations in pyrite indicate progressive cooling from ~400 °C to ~270 °C (Py1 to Py3). Combined with thermodynamic modeling and mineral assemblage constraints, this suggests that the ore-forming fluid experienced significant meteoric water input, accompanied by decreasing temperature, sulfur fugacity, and oxygen fugacity, as well as increasing pH. The principal gold mineralization stage occurred at approximately 340 °C, where temperature and pH conditions jointly stabilized Au transport primarily as $Au(HS)_2^-$. We propose the mixing between meteoric water and mineralized magmatic fluid caused a decrease in sulfur fugacity, oxygen fugacity and temperature, thereby limiting the availability of HS^- required for stabilizing $Au(HS)_2^-$ complexes and thus resulting in the decoupling of $Au(HS)_2^-$, which triggered gold precipitation.

Keywords: Tibet; Xiongcun ore district; Dongga Au deposit; pyrite trace element; mechanism of gold precipitation

Check for updates

Academic Editor: Manuel Munoz

Received: 31 March 2026
Revised: 1 May 2026
Accepted: 12 May 2026
Published: 17 May 2026

Copyright: © 2026 by the authors. Licensee MDPI, Basel, Switzerland. This article is an open access article distributed under the terms and conditions of the Creative Commons Attribution (CC BY) license.

1. Introduction

Epithermal deposits represent an important member of a porphyry mineralization system [1,2], and understanding their metallogenic mechanisms is therefore critical for deciphering the hydrothermal systems of the porphyry mineralization evolution process. However, fluid inclusions of ore-forming quartz in epithermal deposits are commonly small in size (typically <5 μm), and most of quartz is cryptocrystalline [3,4], which makes it difficult to constrain ore-forming fluid characteristics and limits our understanding

of the fluid evolution and metal precipitations. In contrast, pyrite is the most common sulfide in metal hydrothermal deposits, and is commonly coeval or associated with gold mineralization. Trace elements in pyrite have been widely demonstrated to serve as effective tracers of the physicochemical conditions of hydrothermal systems, as well as indicators of fluid evolution and metal precipitation [5–9]. For example, Se concentrations in pyrite can serve as a tracer for estimating ore-forming fluid temperatures [10]. In addition, Co and Ni systematics provide important constraints on pyrite genesis and the characteristics of ore-forming fluids, as their enrichment in pyrite generally reflects a magmatic–hydrothermal source and their Co/Ni ratios are sensitive to fluid composition and physicochemical conditions, including temperature and fluid evolution processes [11]. And such applications have been demonstrated in porphyry–epithermal systems, such as the Xiongcun No. 1 Cu-Au deposit and Zhunuo Cu deposit [12,13], where pyrite trace element geochemistry has been used to constrain fluid evolution and ore-forming processes.

The Xiongcun Cu-Au ore district is located in the central segment of the Southern Lhasa terrane, and consists of the No. 1, No. 2, and No. 3 porphyry Cu-Au deposits and Dongga Au deposit [14]. As the only recognized porphyry–epithermal system in the Southern Lhasa terrane related to Neo-Tethyan subduction [15], it provides key insights into the fluid evolution of porphyry and epithermal mineralization during this tectonic stage. Lang et al. [16] conducted a comprehensive study on the Dongga Au deposit about sources of mineralizing fluids and materials and the connection with the No. 2 porphyry-type mineralization. However, due to the lack of quartz and other minerals suitable for fluid inclusion studies during the gold mineralization stage, the evolution process of the ore-forming fluids and the mechanisms of gold precipitation are still unclear. On the contrary, pyrite is a pervasive mineral in the Dongga Au deposit and is closely associated with gold mineralization, making it an ideal tracer for constraining the evolution of the ore-forming fluids and the mechanisms of gold precipitation.

In this study, we focus on pyrite from the Dongga Au deposit and carry out LA-ICP-MS in situ trace element analysis, providing more precise constraints on the characteristics and evolution of ore-forming fluids, including their chemical evolution (temperature, sulfur fugacity (fS_2), oxygen fugacity (fO_2), and pH) and the role of physical processes such as meteoric water mixing. These results will further contribute to our understanding of the genetic relationships of porphyry–epithermal systems.

2. Regional Geology

The Himalayan–Tibetan Plateau is composed, from north to south, of the Qaidam-Kunlun, Songpan-Ganzi, Qiangtang, Lhasa, and Himalayan terranes (Figure 1b) [17]. The collision between the Indian and Asian plates occurred during 65 to 60 Ma, marking the beginning of the uplift of the Himalayan–Tibetan Plateau and initiating a series of subsequent orogenic processes that ultimately led to the formation of the largest and highest plateau on Earth [18–21].

The Lhasa terrane is located along the southern margin of the Himalayan–Tibetan Plateau and can be further subdivided into the Northern, Central, and Southern Lhasa subterranes by the Shiquan River–NamTso mélange zone (SNMZ) and the Luobadui–Milashan Fault (LMF) (Figure 1c) [22,23]. Characterized by predominantly juvenile crust, the Northern Lhasa terrane (NLT) contains principal stratigraphic units represented by the Early Cretaceous Qushenla and Duoni formations [22,24], while extensive partial melting of its juvenile lower crust during the same period generated voluminous granitoid batholiths [22,25]. The Central Lhasa Terrane (CLT) contains Precambrian basement rocks [22,26,27]. The dominant volcanic rocks include the Zenong Group and the Linzizong Group (comprising the Dianzhong, Pana, and Nianbo formations), which were formed dur-

ing the Late Jurassic to Early Cretaceous and the Paleocene to Eocene, respectively [28,29]. Intrusive rocks are predominantly of the Mesozoic and are distributed along the southern margin of the central segment of the CLT [22,30,31]. The Southern Lhasa terrane (SLT) mainly consists of juvenile crust, although remnants of Precambrian basement rocks are locally preserved [32]. The SLT is composed predominantly of Middle Triassic to Middle Jurassic, and Paleocene to Eocene volcano–sedimentary successions, and Middle Triassic to Miocene batholiths [22,28,33–38]. Intrusive rocks are concentrated in its central and eastern segments, with major emplacement episodes during the Middle Triassic–Late Jurassic, Late Cretaceous, Paleocene–Eocene, and Oligocene–Miocene [34]. They are composed mainly of granitoids, particularly granite and granodiorite [22,39].

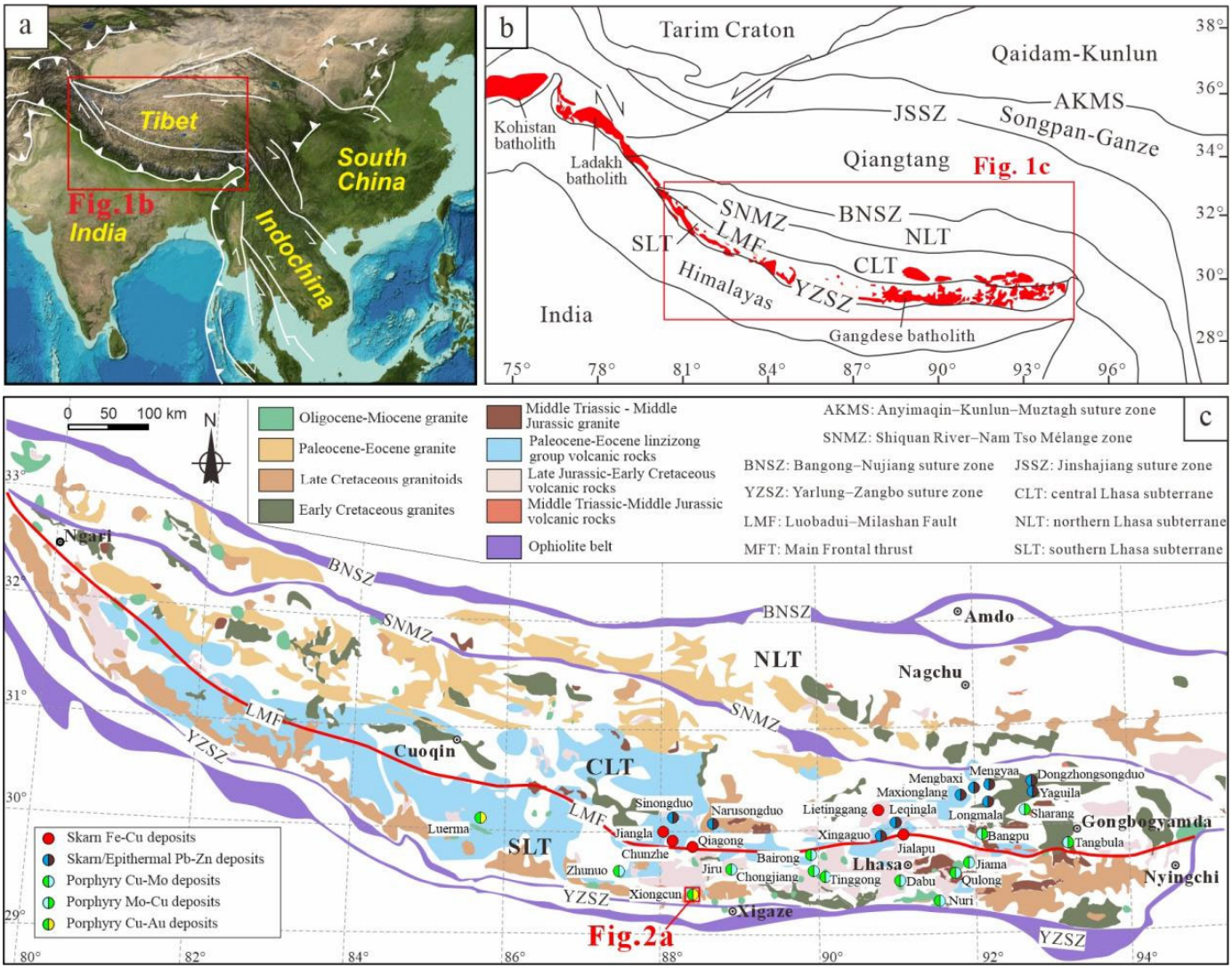


Figure 1. (**a**) Simplified map showing the location of Himalayan–Tibetan orogen. (**b**) Tectonic framework of the Lhasa terrane [22]. (**c**) Geological map of the Lhasa terrane, showing the distribution of magmatic rocks and the associated deposits [22,27].

The SLT experienced early subduction of the Neo-Tethyan Ocean and subsequently collision between the Indian and Asian continents [18,21,34,37,40]. Two major mineralization episodes related to the tectonic events occurred during the Late Triassic–Middle Jurassic and the Miocene, respectively. The Late Triassic-to-Middle Jurassic mineralization corresponds to the northward subduction of the Neo-Tethyan Ocean and is represented by the Xiongcun giant Cu-Au ore district, which hosts the No. 1, No. 2, and No. 3 deposits,

as well as the Dongga Au deposit [14,16,41–43]. In addition, Cu-Au mineralization of this stage also occurs in the Luerma area in the western segment of the Southern Lhasa terrane [44]. During the Miocene, lithosphere delamination or/and break-off of the Indian plate in the post-collisional stage triggered the most significant mineralization event in the Southern Lhasa terrane, resulting in the formation of a series of giant porphyry Cu-Mo deposits, including Jiama, Qulong, Zhunuo, and Bangpu [45–48].

3. Ore Deposit Geology

3.1. Geology of the Xiongcun Ore District

The Xiongcun ore district is located along the southern margin of the central segment of the Southern Lhasa terrane (Figure 1c) [15]. Three porphyry Cu-Au deposits (the No. 1, No. 2, and No. 3 deposits), the Dongga epithermal Au deposit, and several mineralized prospects (e.g., Zemoduola and Donggapu) have been identified within this district (Figure 2a) [16,49–51]. The exposed strata in the Xiongcun ore district mainly comprise the Lower–Middle Jurassic Xiongcun Formation and Quaternary (Figure 2a). The Xiongcun Formation (195 to 165 Ma) [41] mainly consists of volcanic conglomerate, volcanic breccia, tuff, shale, sandstone, siltstones and limestone, with orebodies predominantly hosted in tuff [51]. The Xiongcun ore district records intense magmatism, marked by multiple intrusive phases emplaced during the Early Carboniferous, Jurassic, and Eocene (Figure 2a), including Early Carboniferous hornblende gabbro (~354.9 ± 0.9 Ma) [52], amphibolite (~354.9 ± 0.9 Ma; Wang et al., 2020) and diorite (~354.3 ± 1.4 Ma) [52]; Early Jurassic quartz diorite porphyry (~175.7 Ma) [14]; Early–Middle Jurassic quartz diorite porphyry (174 ± 1.6 Ma) [14]; Middle Jurassic quartz diorite porphyry (~161.8 Ma) [14] and diabase dike (165.3 ± 1.0 Ma) [53]; and Eocene quartz diorite pluton (50 Ma) [50], biotite granodiorite (48 Ma) [50] and lamprophyre dike (47.0 ± 0.6 Ma) [39].

The ore district is characterized by well-developed fault systems, with the E-W-striking F1 and F2 faults forming the principal structures along its southern part. These faults are crosscut by a series of younger N-S- and NE-SW-trending faults. To the north of the F1 fault, an anticline developed with a core composed predominantly of siltstone (Figure 2a).

Two mineralization events occurred within the district in the Early and Middle Jurassic [14,16]. The emplacement of Early Jurassic quartz diorite porphyry resulted in the formation of the No. 2 and No. 3 deposits, as well as the Dongga Au deposit. The No. 2 and No. 3 deposits are characterized by potassic, sodic–calcic, chlorite–sericite, and phyllic alteration. Multiple generations of veins have been identified, including quartz–sulfide veins, magnetite–sulfide veins, quartz–molybdenite–sulfide veins, biotite–sulfide veins, chlorite–sulfide veins, and actinolite veins [41–43]. The emplacement of Middle Jurassic quartz diorite porphyry resulted in the formation of the No. 1 deposit, which is characterized by potassic and phyllic alteration. The principal vein types include early quartz–sulfide veins, biotite–sulfide veins, quartz–sulfide veins, magnetite–sulfide veins, and polymetallic veins [12,54].

3.2. Geology of Dongga Au Deposit

The Dongga Au deposit is located in the central part of the Xiongcun ore district, in close proximity to the No. 2 porphyry Cu-Au deposit (Figure 2a), and they constitute a porphyry–epithermal mineral system [16]. The orebodies of the Dongga Au deposit are hosted within Xiongcun Formation tuffs and occur as a series of subparallel veins extending vertically for approximately 150 m. These veins strike NE-SW and are clearly controlled by NW-SE-trending fractures (Figure 2b,c). The Dongga deposit contains a total of 9.55 t of gold resources, with grades ranging from 0.13 to 61.6 g/t (average grade of

6.9 g/t) [16]. The tuffs are intensely phyllic-altered, and consist mainly of sericite, quartz, and disseminated pyrite (Figure 3).

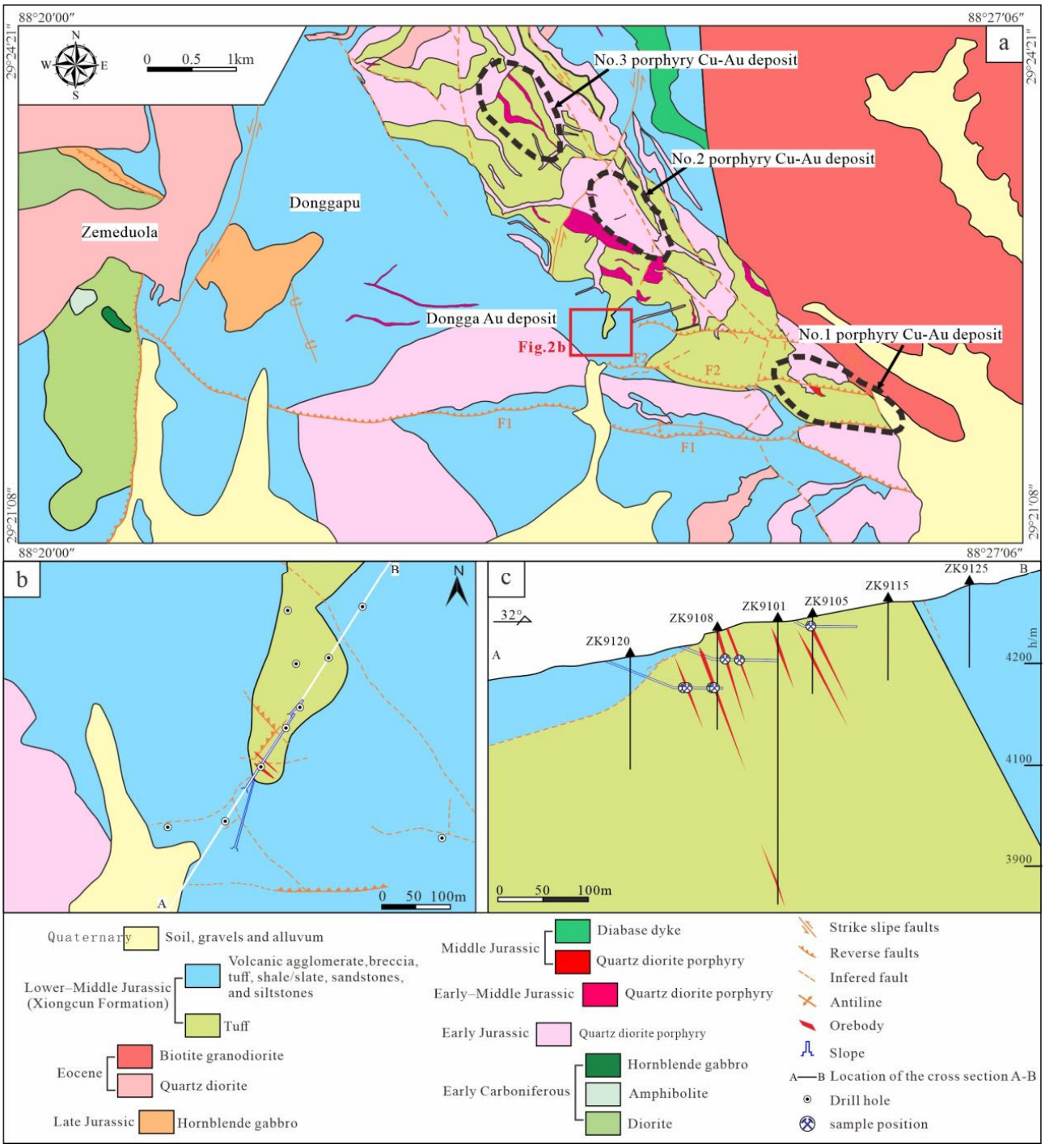


Figure 2. (**a**) Geological map of the Xiongcun ore district [14]. (**b**) Geological map of the Dongga Au deposit. (**c**) Cross-section A–B (see (**b**)) of the Dongga Au deposit [55].

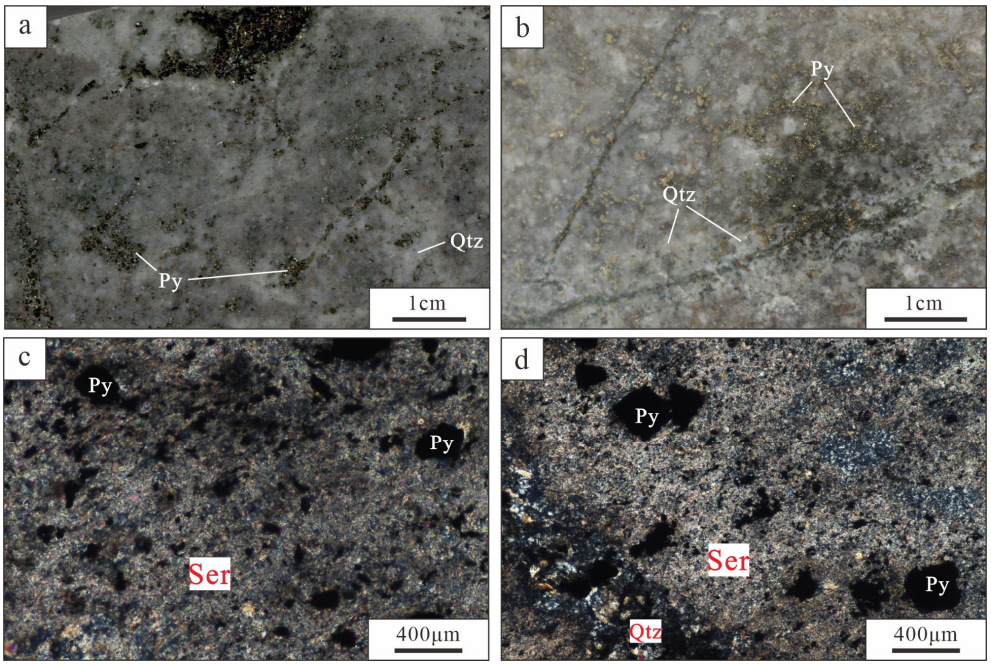


Figure 3. Photographs and microphotographs showing phyllic alteration at Dongga Au deposit. (**a**,**b**) Hand specimens of ore-bearing tuff showing intense phyllic alteration. (**c**,**d**) Microphotographs showing abundant sericite and disseminated pyrite. Py, pyrite; Qtz, quartz; Ser, sericite.

The ore primarily occurs in vein and veinlet forms. Based on crosscutting relationships, five types of veins were identified in the Dongga Au deposit: quartz–sulfide veins, chlorite–sulfide veins, pyrite veins, actinolite veins, and late quartz veins (Figure 4). Quartz–sulfide veins (QSVs) are composed predominantly of quartz and pyrite, with widths ranging from 0.5 to 2 cm (Figure 5a). Chlorite–sulfide veins (CSVs) constitute the principal ore-bearing vein type in the deposit and typically range from 0.2 to 1.5 cm in width, containing pyrite, native gold, electrum, chalcopyrite, pyrrhotite, sphalerite, and magnetite, with chlorite, epidote, and sericite as the main gangue minerals (Figure 5c–i). Pyrite veins (PVs) are dominated by pyrite, with minor chalcopyrite, and are typically 0.5 to 3 cm thick (Figure 5j). Actinolite veins (AVs) are devoid of metallic mineral precipitation and consist mainly of actinolite, chlorite, and epidote, with widths of 0.5 to 1 cm (Figure 5k). Late quartz veins (LQVs) represent the youngest vein generation and consist of quartz with minor calcite; they are typically thin, with widths generally less than 1 cm (Figure 5l).

Based on mineral assemblages and the crosscutting relationships of veins, four hydrothermal mineralization stages (Stage A, Stage B, Stage C and Stage D) and one supergene stage were identified (Figure 6). Stage A is dominated by quartz, sericite, and minor pyrite. Stage B represents the principal gold mineralization stage and can be further subdivided into two sub-stages (B1 and B2) based on mineral assemblages. Stage B1 is characterized by the precipitation of pyrite, chalcopyrite, pyrrhotite and gold minerals (native gold and electrum), accompanied by minor sphalerite. During Stage B2, magnetite commonly replaces the early-formed pyrite and chalcopyrite. Minor sericite, together with chlorite and epidote, form continuously throughout Stage B. Stage C is characterized by the formation of abundant pyrite and minor chalcopyrite. Stage D represents the late hydrothermal stage of the Dongga Au deposit and is marked by the development of AV and LQV. It is characterized by quartz, actinolite, chlorite, and epidote, accompanied by minor sericite and calcite.

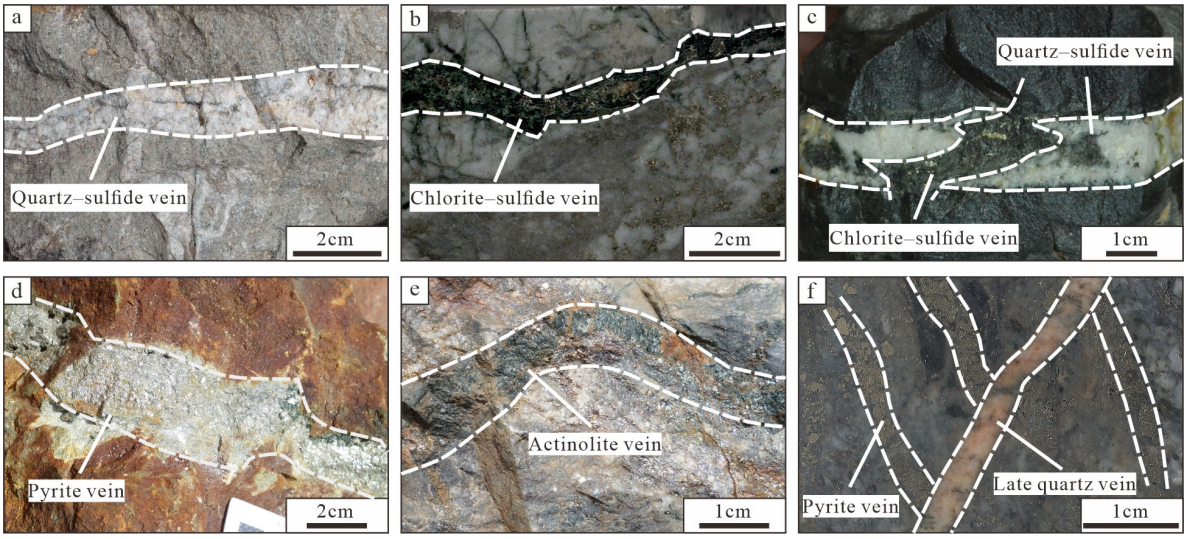


Figure 4. Representative photographs showing the typical vein types in the Dongga Au deposit. (**a**) Quartz–sulfide vein. (**b**) Chlorite–sulfide vein. (**c**) Quartz–sulfide vein crosscut by chlorite–sulfide vein. (**d**) Pyrite vein. (**e**) Actinolite vein. (**f**) Pyrite vein crosscut by late quartz vein.

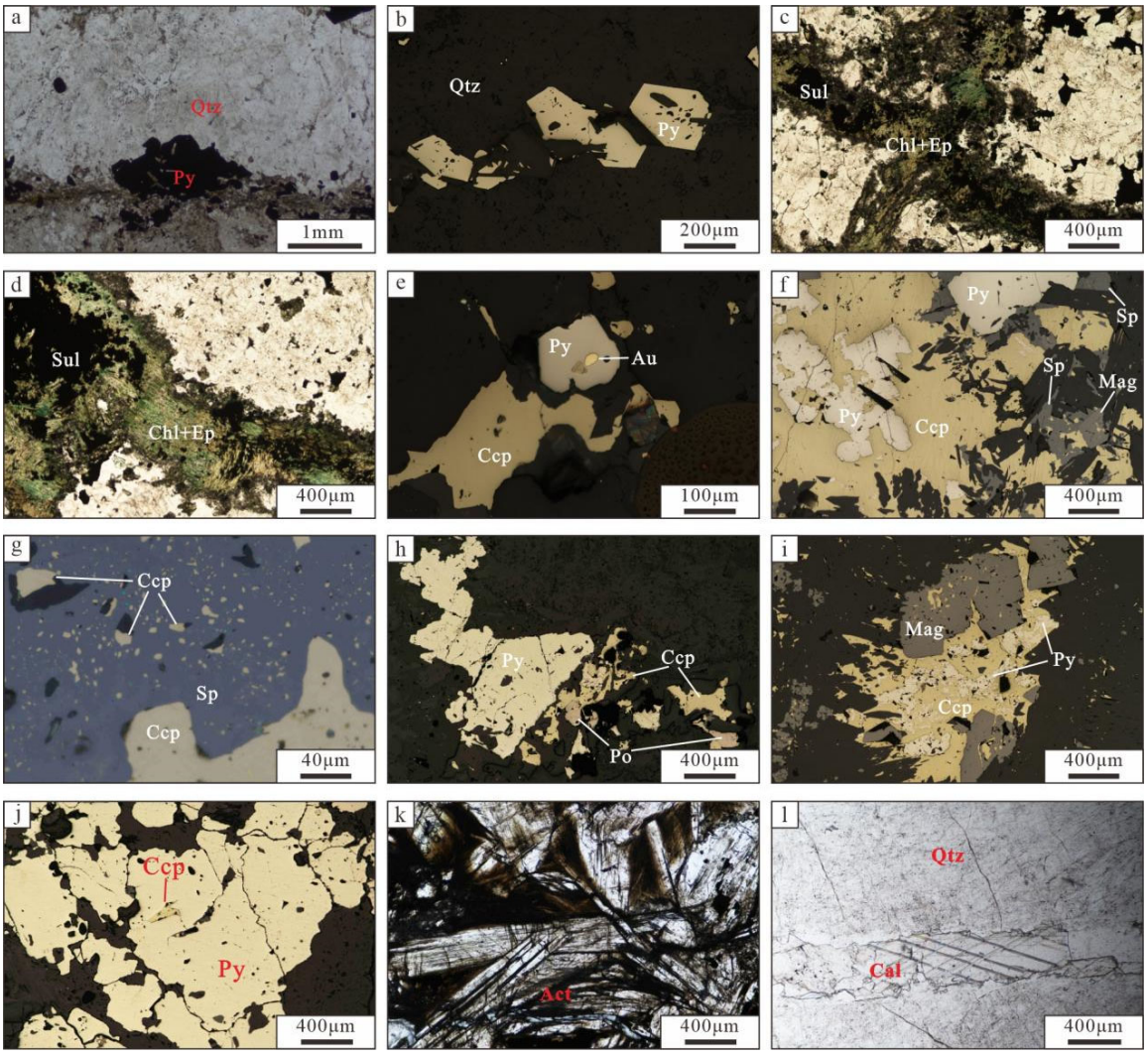


Figure 5. Photomicrographs illustrating ore textures and mineral assemblages. (**a**) Quartz and pyrite in quartz–sulfide vein. (**b**) Subhedral to anhedral pyrite. (**c**,**d**) Chlorite, epidote, and sulfides in chlorite–

sulfide vein. (**e**) Native gold in pyrite. (**f**) Pyrite, chalcopyrite, sphalerite, and magnetite in chlorite–sulfide vein. (**g**) Chalcopyrite disease in sphalerite. (**h**) Co-existence of pyrrhotite with pyrite and chalcopyrite in chlorite–sulfide vein. (**i**) Magnetite replacement for pyrite and chalcopyrite in chlorite–sulfide vein. (**j**) Anhedral pyrite and minor chalcopyrite in pyrite vein. (**k**) Actinolite in actinolite vein. (**l**) Quartz and minor calcite in late quartz vein. Py, pyrite; Po, pyrrhotite; Ccp, chalcopyrite; Sp, sphalerite; Mag, magnetite; Sul, sulfide; Au, native gold; Qtz, quartz; Chl, chlorite; Ep, epidote; Act, actinolite; Cal, calcite.

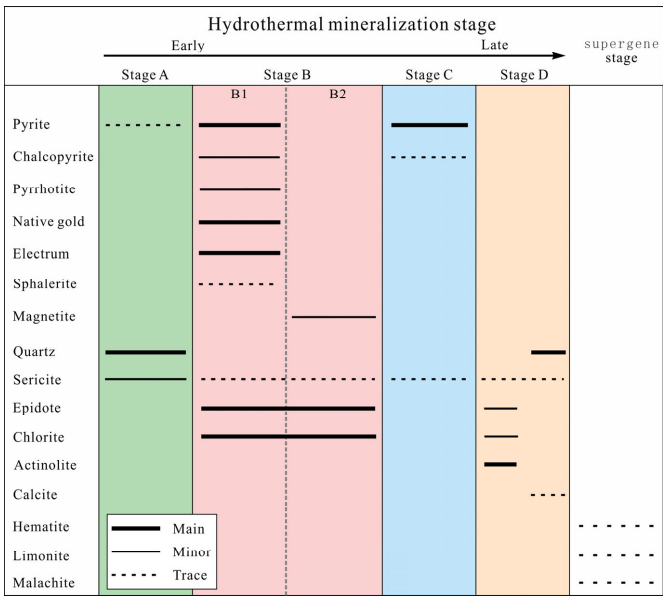


Figure 6. Mineral paragenetic sequence for the Dongga Au deposit.

4. Samples and Analytical Methods

A total of seven samples were selected from the Dongga Au deposit for this study, including three QSV samples, three CVS samples, and one PV sample. The specific locations of sampling are shown in Figure 2c. All samples were prepared as thin sections for detailed petrographic examination. Representative pyrite grains from selected samples were subsequently chosen for in situ LA-ICP-MS trace element analysis. The following elements were detected: ^{59}Co, ^{60}Ni, ^{63}Cu, ^{66}Zn, ^{72}Ge, ^{75}As, ^{78}Se, ^{107}Ag, ^{121}Sb, ^{125}Te, ^{197}Au, ^{208}Pb and ^{209}Bi.

Trace element analysis of sulfides was conducted by LA-ICP-MS at Wuhan SampleSolution Analytical Technology Co., Ltd., Wuhan, China. Detailed operating conditions for the laser ablation system, the ICP-MS instrument, and data reduction are the same as those described by Zong et al. [56]. Laser sampling was performed using a GeolasPro laser ablation system (Coherent Inc., California, USA; manufactured in Germany) that consists of a COMPexPro 102 ArF excimer laser (wavelength of 193 nm and maximum energy of 200 mJ) and a MicroLas optical system. An Agilent 7900 ICP-MS instrument (Agilent Technologies, California, USA; manufactured in Japan) was used to acquire ion-signal intensities. Helium was applied as a carrier gas. Argon was used as the make-up gas and mixed with the carrier gas via a T-connector before entering the ICP. A "wire" signal smoothing device is included in this laser ablation system [57]. The spot size and frequency of the laser were set to 32 μm and 5 Hz, respectively, in this study. Trace element compositions of sulfides were calibrated against various reference materials (NIST 610, developed by the National Institute of Standards and Technology, USA) without using an internal standard [58]. The sulfide reference material of Table S2 MASS-1 (USGS) was used as the unknown sample to verify the accuracy of the calibration method. Each analysis incorporated a background acquisition of approximately 20–30 s followed by 50 s of data acquisition from the sample.

Excel-based software, ICPMSDataCal 11.8, was used to perform off-line selection and integration of background and analyzed signals, time-drift correction, and quantitative calibration for trace element analysis [58]. The detection limit of Co was 0.0086 ppm, that of Ni was 0.3201 ppm, that of Cu was 0.0886 ppm, that of Zn was 0.0618 ppm, that of Ge was 0.2624 ppm, that of As was 0.5308 ppm, that of Se was 8.2374 ppm, that of Ag was 0.0112 ppm, that of Sb was 0.0132 ppm, that of Te was 0.0363 ppm, that of Au was 0.0072 ppm, that of Pb was 0.0066 ppm, and that of Bi was 0.0041 ppm. And analytical precision and reproducibility were generally within a 3%–15% relative standard deviation (RSD) for most trace elements.

5. Results

5.1. Petrography of Pyrite

Pyrite represents the dominant sulfide in the Dongga Au deposit and occurs throughout Stages A, B, and C. Based on petrographic observations and paragenetic relationships, three generations of pyrite were identified.

The first-generation pyrite (Py1) formed during Stage A and occurs within QSVs. It typically exhibits subhedral to anhedral crystal forms with grain sizes ranging from ~100 to 500 μm and is closely associated with quartz (Figure 7a,b). The second-generation pyrite (Py2), precipitated during Stage B, occurs in CSVs as subhedral to anhedral crystals reaching up to ~1 mm in size. Py2 is closely associated with gold mineralization and is locally replaced by late pyrrhotite and magnetite (Figure 7c,d). The third-generation pyrite (Py3) formed during Stage C and predominantly occurs in pyrite veins as anhedral crystal (Figure 7e,f).

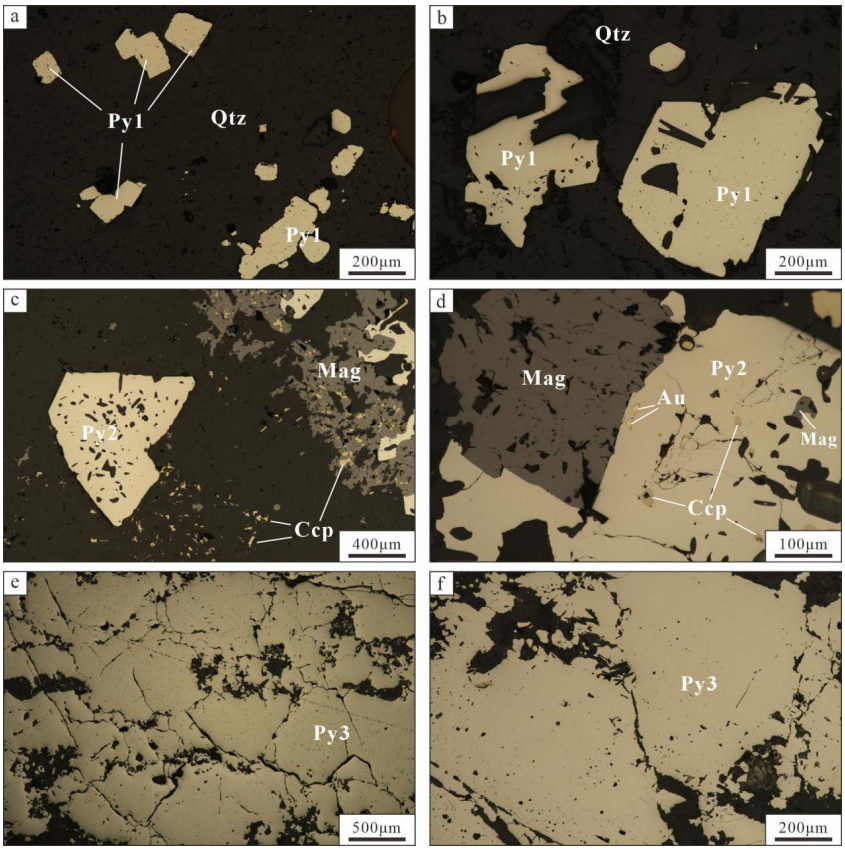


Figure 7. Microphotographs showing the different generations of pyrite. (**a**,**b**) Subhedral to anhedral Py1 in Stage A. (**c**,**d**) Subhedral to anhedral Py2 of Stage B with chalcopyrite and native gold, which were replaced by later magnetite. (**e**,**f**) Anhedral Py3 in Stage C. Py, pyrite; Ccp, chalcopyrite; Mag, magnetite; Qtz, quartz.

5.2. Trace Elements in Pyrite

A total of 129 in situ LA-ICP-MS analyses were conducted on pyrite from the Dongga Au deposit, and the analytical elements were Au, Ag, Sb, Cu, Zn, Te, Bi, Pb, Co, As, Ni and Se (Figure 8). All results are provided in Supplementary Table S1. The LA-ICP-MS sulfide analyses can be affected by the presence of micro-scale inclusions containing various elements. As a result, all LA-ICP-MS spectra were inspected for the presence of spikes indicating mineral inclusions, and the LA-ICP-MS data set for each sulfide was filtered.

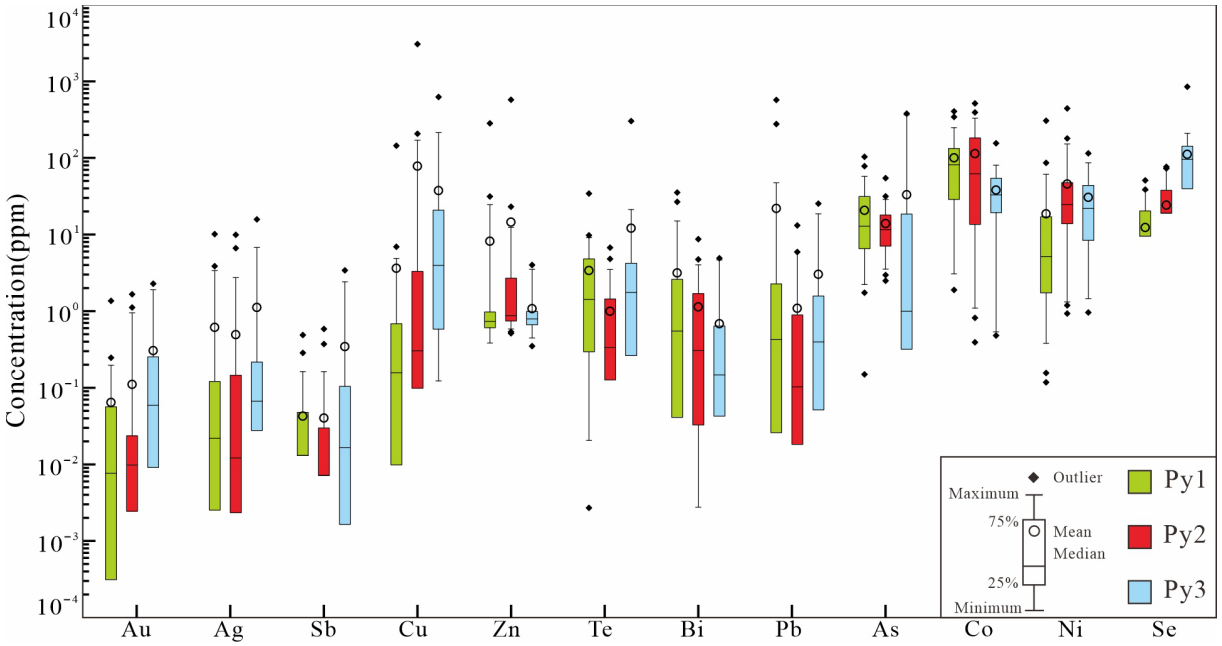


Figure 8. Box and whisker plots of trace element compositions in different types of pyrite. All results are available in Supplementary Table S1.

Au and Ag occur at uniformly low concentrations across all three pyrite generations. Au shows a slight increase from Py1 to Py2 and Py3, whereas Ag exhibits no clear stage-dependent trend. In Py1, Au contents range from <LOD to 1.36 ppm with a mean value of 0.11 ppm, and Ag contents range from <LOD to 10.11 ppm with a mean value of 0.89 ppm. In Py2, Au contents range from <LOD to 1.65 ppm (mean = 0.17 ppm), and Ag contents range from <LOD to 9.93 ppm (mean = 0.82 ppm). Py3 show the highest Au and Ag contents, ranging from <LOD to 2.27 ppm (mean value of 00.35 ppm) and <LOD to 15.78 ppm (mean value of 1.32 ppm), respectively (Figure 8).

Co concentrations are comparable in Py1 (mean = 102.14 ppm) and Py2 (mean = 113.38 ppm) but decrease markedly in Py3 (mean = 38.00 ppm). In contrast, Ni exhibits an overall increasing trend from Py1 to Py2, with mean values rising from 19.39 ppm in Py1 to 45.66 ppm in Py2, and remaining at 30.48 ppm in Py3 (Figure 8).

Chalcophile base metals (Cu, Zn, and Pb) display distinct distribution patterns among the three pyrite generations. Cu concentrations increase progressively from Py1 (mean = 5.60 ppm) to Py2 (mean = 96.80 ppm) and Py3 (mean = 38.58 ppm). Zn is enriched in Py1 (mean = 8.51 ppm) and Py2 (mean = 14.48 ppm) but shows a marked decrease in Py3 (mean = 1.08 ppm). Pb exhibits the highest mean concentration in Py1 (mean = 24.45 ppm), whereas markedly lower mean values are observed in Py2 (mean = 1.22 ppm) and Py3 (mean = 3.32 ppm) (Figure 8).

Arsenic concentrations remain generally low and show limited inter-stage variability. In Py1, As contents mainly range from <LOD ppm to 103.63 ppm with a mean value of 21.13 ppm. In Py2, As ranges from 2.49 to 54.43 ppm (mean = 13.88 ppm). Py3 displays the highest As

concentrations, ranging from <LOD to 379.07 ppm with a mean value of 57.29 ppm. Sb, Te, and Bi generally occur at low concentrations across all three pyrite generations and show only minor inter-stage variability (Figure 8). Mean contents remain within 0.08 to 0.52 ppm for Sb, within 1.00 to 12.07 ppm for Te, and within 0.68 to 3.14 ppm for Bi, without pronounced trends. In contrast, Se exhibits well-defined and systematic variation among stages. Se concentrations increase progressively from Py1 (mean = 12.34 ppm) to Py2 (mean = 24.12 ppm) and reach the highest values in Py3 (mean = 111.14 ppm) (Figure 8).

6. Discussion

6.1. Occurrence of Trace Elements in Pyrite

Pyrite hosts a wide range of trace elements (e.g., Au, As, Co, Ni, Pb, Zn, Se, etc.), which occur predominantly in three forms: (1) as solid solution in the pyrite lattice, (2) as invisible sulfide nanoparticles, and (3) as micro-scale mineral inclusions [8,10,59,60]. In the case of smooth LA-ICP-MS time-resolved depth profiles, a solid solution or homogeneous distribution of mineral particles can result in smooth laser ablation spectra [61], while larger particles can be recognized as spikes in the LA-ICP-MS time-resolved depth profiles (Figure 9).

Compared with most other trace elements, Au concentrations are relatively low and are broadly similar across the three generations of pyrite (Figure 8). Generally, invisible gold in pyrite may occur in two forms: (1) micro- to nanoparticle Au^0, which refers to independent Au minerals such as native gold and electrum, and (2) isomorphous Au^+/Au^{3+}, where Au substitutes cations (e.g., Fe^{2+}) in the pyrite lattice and exists in the form of a solid solution [59,62–64]. At Dongga, Au concentrations across the three generations of pyrite exhibit no obvious correlation with Ag or Sb (Figure 10a,b), suggesting that Au is unlikely to occur as discrete mineral phases (such as native gold and electrum) within pyrite. Moreover, all analyses plot below the Au solubility line in the Au–As diagram (Figure 10c), indicating that Au is unlikely to be present as nanoparticulate Au^0 and is most likely incorporated into the pyrite lattice in Au^+ [8,10,58]. In addition, Au and As exhibit similar LA-ICP-MS signal patterns (Figure 9e,f), which provides additional evidence for the interpretation above.

Pb is least likely to be incorporated into the pyrite lattice, because Pb^{2+} has a larger ionic radius than Fe^{2+} [65]. Furthermore, Pb has a faster precipitation rate from an aqueous solution as a metal sulfide compared to Fe [6,66]. As a result, Pb commonly occurs as nano- to micro-scale inclusions in pyrite. Consistent with this interpretation, the spiky LA-ICP-MS signal patterns of Pb, similar to those of Ag and Bi, observed in pyrite from the Dongga Au deposit (Figure 9), together with the significant positive correlations among Ag, Pb, and Bi (Figure 10d–f), indicate that these elements are hosted mainly in micro-inclusions within pyrite, probably in the form of bismuthinite and galena.

Similarly to Pb, Zn and Cu are also not easily incorporated into the pyrite lattice but are preferentially hosted as mineral inclusions, typically occurring as sphalerite and chalcopyrite [67]. In the LA-ICP-MS time-resolved depth profiles, Cu and Zn display similar peak patterns (Figure 9b,c), providing support for this interpretation and indicating that these elements occur as chalcopyrite and sphalerite inclusions within pyrite rather than being incorporated into the lattice by isomorphism. In addition, petrographic observations reveal chalcopyrite exsolution textures within sphalerite (Figure 5g), providing independent mineralogical evidence for the presence of sphalerite and associated Cu-Zn sulfide assemblages in the hydrothermal system. Although these observations represent macroscopic mineral textures, similar Cu-Zn sulfide assemblages could also occur at finer scales and be subsequently entrapped by pyrite, accounting for the Cu-Zn signatures observed in the time-resolved LA-ICP-MS profiles.

Cobalt (Co), Ni and As are commonly distributed in pyrite, and in the LA-ICP-MS time-resolved depth profiles, most samples showed flat signal patterns for these elements as well as for Fe (Figure 9), suggesting that Co, Ni and As appear in the pyrite lattice through isomorphism. In addition, the similar time-resolved signal patterns of As and Au (Figure 9e,f) suggest that As is most likely incorporated into pyrite by substituting S^{-} with As^{-}, thereby facilitating the incorporation of Au into the pyrite structure.

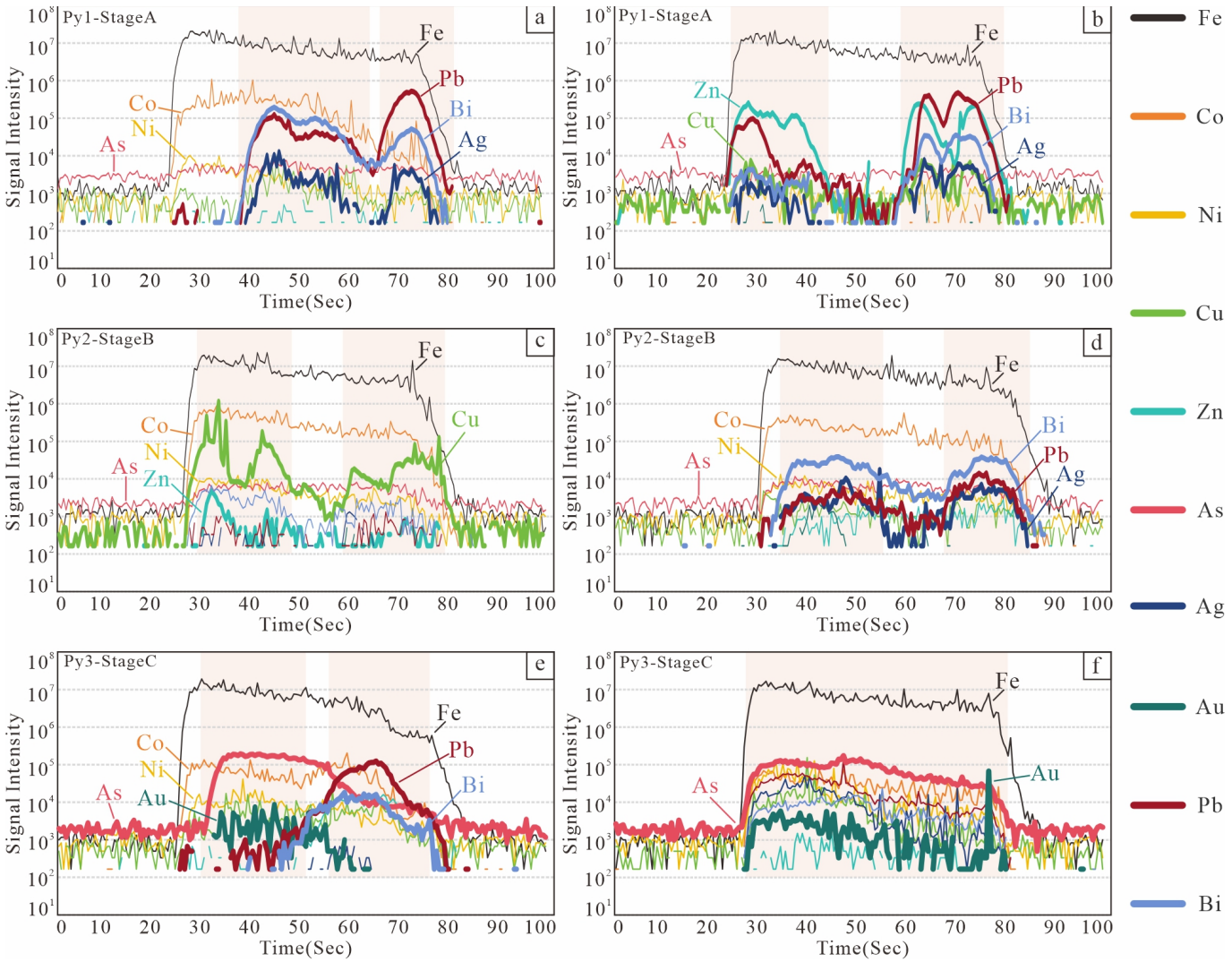


Figure 9. Representative time-resolved LA-ICP-MS depth profiles of the pyrite analyzed in this study, indicating the occurrence of major metal elements. Fe has a relatively flat principal element response, indicating homogeneous pyrite. In most samples, Co, Ni, and As exhibit flat LA-ICP-MS time-resolved signal patterns similar to that of Fe, indicating that these elements are incorporated into the pyrite lattice by isomorphism. (**a**) The spiky signal of Pb, Bi and Ag indicates the presence of bismuthinite and galena. (**b**) The spiky LA-ICP-MS signals of Pb, Bi, Ag, as well as Zn and Cu, indicate that these elements are likely hosted in pyrite as micro-inclusions. (**c**) The spiky signal of Cu and Zn indicates the presence of chalcopyrite and sphalerite inclusions. (**d**) The spiky signal of Pb, Bi and Ag indicates the presence of bismuthinite and galena. (**e**,**f**) Au and As display similar LA-ICP-MS signal patterns, suggesting that Au is likely incorporated into the pyrite lattice as lattice-bound gold.

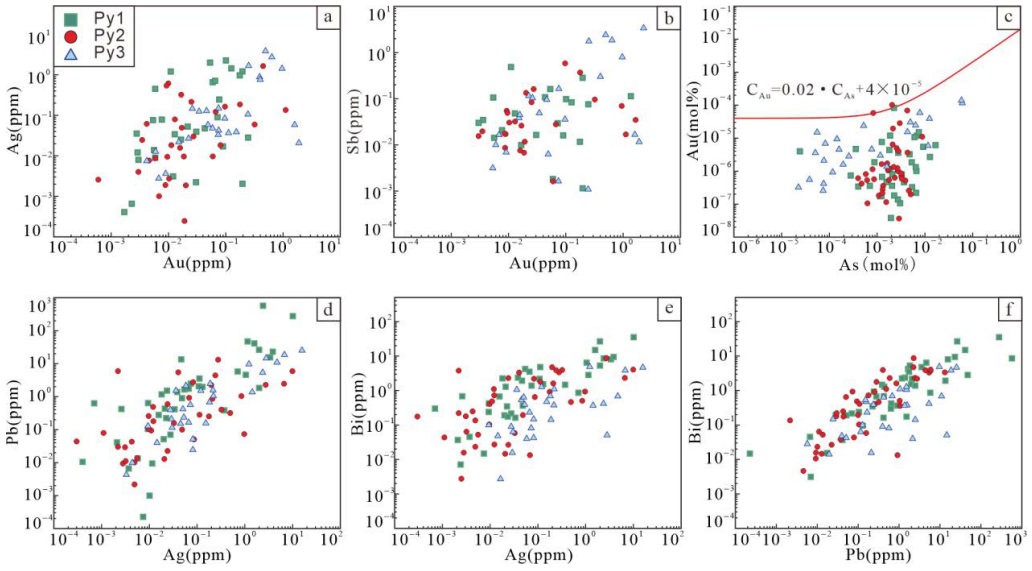


Figure 10. Binary plots of (**a**) Au vs. Ag, (**b**) Au vs. Sb, (**c**) Au vs. As, (**d**) Ag vs. Pb, (**e**) Ag vs. Bi, and (**f**) Pb vs. Bi in different stages of pyrite. The curves in (**c**) represent the solubility limit of Au as a function of As concentrations, as determined by Reich et al. [59].

6.2. Physicochemical Conditions of Mineralization

Variations in pyrite trace element compositions are commonly attributed to evolving physicochemical conditions of ore-forming fluids, including temperature (T), pH, sulfur fugacity (fS_2), and oxygen fugacity (fO_2), owing to the contrasting sensitivities of individual trace elements to these parameters during fluid evolution [8,11,60]. Consequently, trace element concentrations in pyrite provide a proxy for constraining the physicochemical conditions of hydrothermal fluids and for unraveling the mechanisms of fluid evolution and metal precipitation in hydrothermal deposits.

Temperature influences the relative incorporation of Co and Ni into pyrite, with Co tending to be preferentially incorporated at higher temperatures and Ni becoming relatively enriched at lower temperatures [11,68]. In the Dongga deposit, Co concentrations show a slight decreasing trend from Py1 to Py3, whereas Ni concentrations increase markedly (Figure 8), suggesting progressive cooling of the ore-forming fluids. The Co/Ni ratio in pyrite can be influenced by multiple factors, including fluid composition, temperature-dependent partitioning, and the salinity of the hydrothermal solution [69]. Therefore, it is used here only as a qualitative indicator of temperature variation. In the Dongga Au deposit, the Co/Ni ratio shows an overall decrease from Py1 to Py3, with mean values declining from 48.43 to 1.72 (Figure 11), which is consistent with the inferred cooling trend and provides supportive evidence for temperature evolution. In addition, Se incorporation into pyrite is influenced not only by temperature but also by factors such as fluid composition and element partitioning [68]. Nevertheless, empirical relationships between Se concentrations in pyrite and temperature have been proposed [10], providing a useful framework for evaluating relative temperature variations:

$$Se_{pyrite} = 5 \times 10^{13} \times T^{-4.82} \quad (1)$$

In this study, Se concentrations are therefore used as a semi-quantitative proxy to assess temperature evolution. Pyrite shows a marked increase in Se from Py1 to Py3, with mean values rising from ~10 ppm to ~111 ppm (Figure 8), which is consistent with progressive cooling of the ore-forming fluids. Accordingly, temperatures are interpreted to decrease broadly from ~390 °C (Py1; IQR: 364–424 °C) to ~340 °C (Py2; IQR: 314–384 °C)

and ~270 °C (Py3; IQR: 247–308 °C). These estimates are used to constrain the relative temperature trend, and are broadly consistent with the cooling trend inferred from Co–Ni systematics. Together, these geochemical indicators consistently point to progressive cooling of the ore-forming system during mineralization.

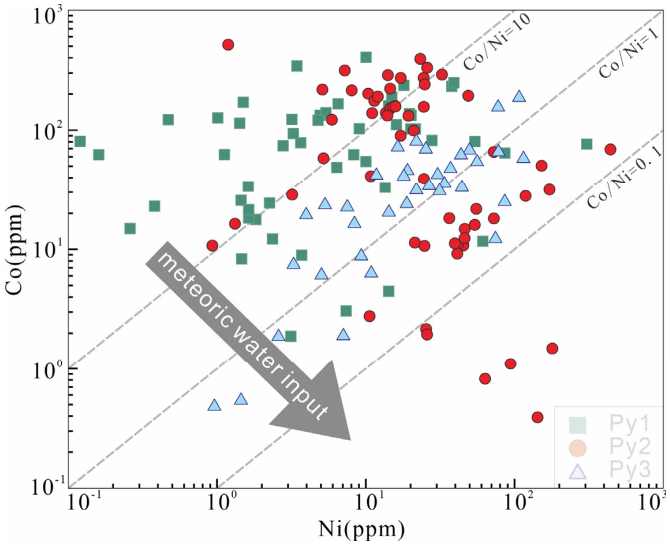


Figure 11. Bivariate variation diagram of Co vs. Ni in different stages of pyrite.

Variations in temperature and sulfur fugacity (fS_2) exert fundamental control on the stability of sulfide mineral assemblages [70]. In this study, the evolution of sulfur fugacity is evaluated qualitatively by integrating estimated temperatures with mineral assemblages. Pyrite from Stage A (Py1) formed at temperatures of approximately ~400 °C, and occurs within QSVs that lack other metal sulfide minerals, indicating that physicochemical conditions were constrained within an intermediate sulfur fugacity range between the arsenopyrite and pyrrhotite buffers (Figure 12). In Stage B1, the decrease in temperature and pyrrhotite precipitated in CSVs marked a transition toward lower sulfur fugacity conditions. This trend continued into Stage B2, where magnetite replaced pyrite, reflecting a sustained decline in sulfur fugacity, approaching a low-sulfur fugacity regime between the pyrrhotite and fayalite stability fields (Figure 12). In Stage C, continued cooling shifted sulfide stability and returned the fluid to the pyrite stability field, leading to the precipitation of Py3 (Figure 12).

In terms of oxygen fugacity, the stability fields of minerals in the Dongga Au deposit were constrained under equilibrium conditions using the pH–oxygen fugacity diagram (Figure 13). For these calculations, mineral phases were treated as ideal solids. The ore-bearing tuffs in the Dongga Au deposit exhibit intense phyllic alteration characterized by abundant sericite. This alteration assemblage constrains the early ore-forming fluid (Stage A) to weakly acidic conditions. Under such pH conditions, pyrite (Py1) represents the stable sulfide phase, placing the fluid within the pyrite stability field (Figure 13a). Thermodynamic calculations further indicate that the stability of epidote and chlorite in the Fe-Cu-S-O system requires pH conditions higher than those of the muscovite stability field [71]. The appearance of chlorite during Stage B therefore reflects a shift in the ore-forming fluid toward more neutral to alkaline conditions relative to Stage A (Figure 13b). Within this pH condition, the precipitation of pyrrhotite during Stage B1 corresponds to fluid conditions entering the pyrrhotite stability field, consistent with a marked decrease in oxygen fugacity. During Stage B2, the formation of magnetite records continued chemical evolution of the fluid toward more alkaline conditions, consistent with the magnetite stability field (Figure 13b). During Stage C, further cooling modifies the sulfide stability

field of pyrite, allowing the fluid to re-enter the pyrite stability field and resulting in renewed precipitation of pyrite (Py3; Figure 13c).

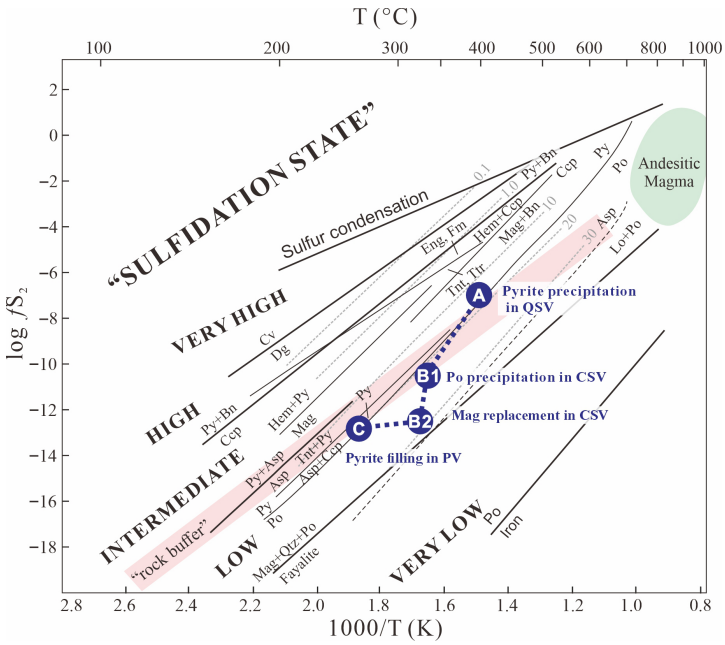


Figure 12. Diagram of log fS_2 vs. 1000/T [70,72], illustrating the evolution of fluid properties during mineralization Stage A to Stage C. The dashed line represents the inferred evolutionary trend rather than a precisely constrained path. Temperature estimates are based on mineral geothermometry, whereas sulfur fugacity is constrained qualitatively based on the stability of sulfide mineral assemblages. These estimates reflect relative changes in physicochemical conditions rather than precise determinations. Abbreviations: Py = pyrite; Bn = bornite; Cv = covellite; Dg = digenite; Eng = enargite; Fm = famatinite; Hem = hematite; Ccp = chalcopyrite; Mag = magnetite; Tnt = tennantite; Ttr = tetrahedrite; Asp = arsenopyrite; Po = pyrrhotite; Qtz = quartz; Lo = loellingite.

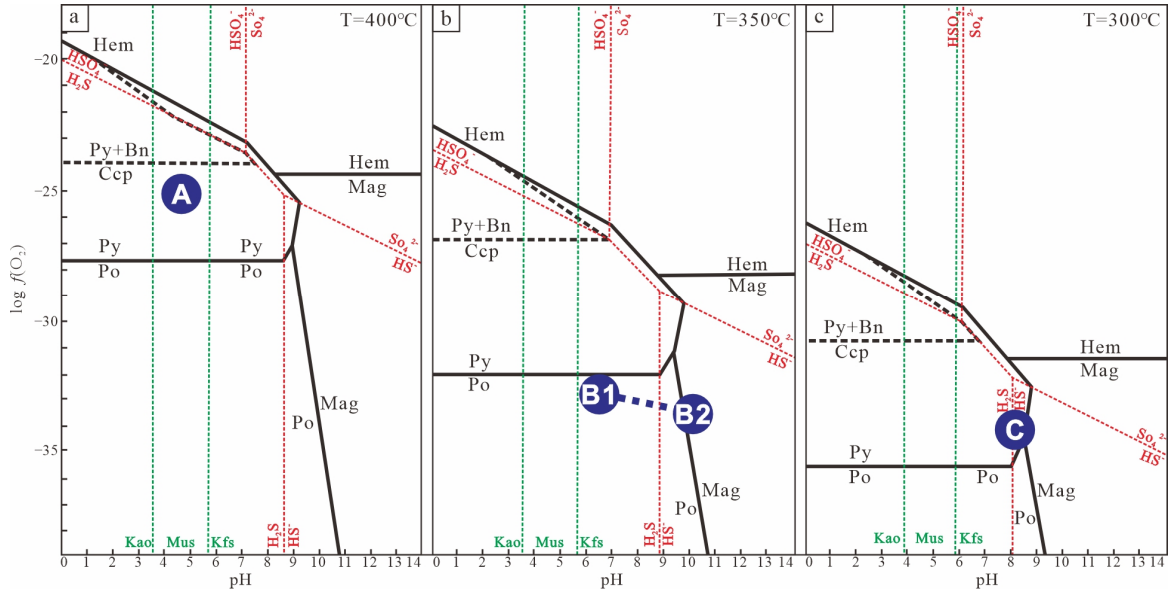


Figure 13. Diagram of log fO_2 vs. pH showing stability fields of minerals in the Cu-Fe-S-O system at (**a**) 400 °C, (**b**) 350 °C and (**c**) 300 °C [73]. Stability fields were calculated in Rstudio 4.4.2 software using the CHNOSZ thermodynamic database, assuming ∑S = 0.001 mol/kg and ∑NaCl = 1 mol/kg. Abbreviations: Py = pyrite; Bn = bornite; Ccp = chalcopyrite; Mag = magnetite; Po = pyrrhotite; Kao = kaolinite; Mus = muscovite; Kfs = K-feldspar.

6.3. Gold Precipitation Mechanism

Gold is typically dissolved and transported in hydrothermal fluids as chloride complexes ($AuCl_2^-$), hydrosulfide complexes ($Au(HS)_2^-$), and in some cases neutral $AuHS^0$ species [74,75]. At relatively high temperatures (>400 °C), Au is predominantly transported as chloride complexes [75]. In contrast, at lower temperatures (<350 °C), hydrosulfide complexes such as $Au(HS)_2^-$ become the primary species in near-neutral fluids, while under weakly acidic conditions, $AuHS^0$ may also play a significant role in Au transport in fluid [75]. Gold mineralization in the Dongga Au deposit primarily occurred during Stage B, at an average temperature of ~350 °C and under near-neutral to alkaline fluid conditions (Figure 13). Thus, we infer that the primary species involved in Au transport was $Au(HS)_2^-$, whose dissolution and precipitation were controlled by the following reaction [76]:

$$Au(HS)_2 + 0.5H_2 + H^+ = Au(s) + 2H_2S \quad (2)$$

Based on this reaction, it is evident that the key to gold precipitation lies in the decoupling of $Au(HS)_2^-$. Under such conditions, wall-rock Fe-sulfidation reactions can promote gold precipitation [77]. However, in both Stage A and Stage C, abundant pyrite precipitation is observed, yet no visible gold is present, nor is there a corresponding increase in Au concentrations in pyrite. Thus, this process is unlikely to have been the dominant mechanism in the Dongga Au deposit.

In addition, fluid boiling [78,79], fluid cooling [80,81], and fluid mixing [82–84] processes can modify the stability of $Au(HS)_2^-$ in hydrothermal systems, ultimately leading to gold precipitation [85–87]. The interpretation of boiling processes relies on the distinct fractionation behavior of trace elements during boiling. Pb and Co are not preferentially transported by ascending hydrothermal fluids and remain in the fluid phase after boiling, whereas elements like Sb and Tl tend to partition into the vapor phase [88]. Therefore, extensive boiling would be expected to result in a depletion of Sb and Tl, while Co and Pb concentrations remain relatively unchanged. However, such geochemical trends are not observed in the pyrite from the Dongga Au deposit (Figure 8), arguing against significant boiling during mineralization. Moreover, if cooling were the dominant mechanism, a decrease in temperature would be anticipated without substantial changes in other physicochemical conditions [80,81]. In contrast, the Dongga Au deposit records significant variations in sulfur fugacity, oxygen fugacity, and pH during the decline in temperature, indicating that cooling alone cannot account for gold precipitation. In addition to constraining temperature, the Co/Ni ratio of pyrite can also provide insights into fluid mixing during ore formation [89–91]. Generally, pyrite of magmatic–hydrothermal origin is commonly characterized by Co/Ni > 1 [89,90]. At Dongga, most Py1 samples display Co/Ni > 1, consistent with a dominantly magmatic–hydrothermal origin for the early-stage fluids [14]. The subsequent decrease in Co/Ni ratios from Py2 to Py3 (Figure 11) may reflect progressive modification of the fluid composition and is consistent with the involvement of meteoric water during mineralization. Further support is provided by the Se/Ge ratios of pyrite, which have been proposed as an effective tracer for distinguishing between magmatic and meteoric fluid sources. Magmatic fluids typically exhibit Se/Ge ratios of ~100, whereas meteoric water-dominated systems are characterized by markedly lower values [92]. In the Dongga Au deposit, pyrite from Py1 and Py2 yields relatively low Se/Ge ratios (with mean values of 10.04 and 18.87, respectively) compared with the magmatic reference value, which is consistent with meteoric water involvement during the early to principal gold mineralization stages. In contrast, Se/Ge ratios increase to 68.41 in Py3, which may suggest a reduced influence of meteoric water during Stage C. Independent evidence for such fluid mixing is also provided by previous fluid inclusion studies [16]. Quartz from the

early quartz–sulfide veins (QSVs) contains both high-salinity S-type fluid inclusions and low-salinity L-type inclusions, which demonstrates that fluid mixing had already occurred during Stage A. Thus, based on the discussion above, we infer that meteoric water mixing, through its modification of the physicochemical conditions of the ore-forming fluid, was the dominant factor driving gold precipitation in the Dongga Au deposit.

Meteoric water mixing significantly alters the physicochemical conditions of hydrothermal fluids, including temperature, sulfur fugacity, oxygen fugacity, and pH [76,85]. And these changes modify the stability of Au-HS complexes and ultimately control gold precipitation [93].

Previous studies have shown that, in hydrothermal systems where Au is transported predominantly as $Au(HS)_2^-$, a decrease in pH promotes gold precipitation by shifting sulfur speciation from HS^- to H_2S, thereby destabilizing Au-HS complexes [93,94]. However, in the Dongga Au deposit, the principal gold precipitation stage (Stage B) was accompanied by a shift toward near-neutral to slightly alkaline conditions, which contrasts with the expected pH-driven gold precipitation mechanism. This apparent discrepancy suggests that pH exerted only a limited effect on the stability of $Au(HS)_2^-$. We therefore infer that pH variation was unlikely to have been the dominant control on gold precipitation at Dongga. In contrast, a decrease in temperature reduces gold solubility and contracts the stability field of Au-bearing complexes, making cooling an efficient mechanism for gold precipitation in hydrothermal systems [93]. Sulfur fugacity directly governs the availability of reduced sulfur species required for gold transport, and a decrease in sulfur fugacity lowers the concentration of HS^- ligands, thereby destabilizing Au-HS complexes and promoting gold precipitation [93,94]. In addition, a decrease in oxygen fugacity can further facilitate gold precipitation by shifting sulfur speciation and destabilizing Au-S complexes [93,95]. These relationships are consistent with the decreases in sulfur fugacity, oxygen fugacity, and temperature during Stage B, which coincided with the principal gold precipitation event. Collectively, the decline in sulfur fugacity and temperature reduced HS^- availability in the ore-forming fluid, whereas the decrease in oxygen fugacity further modified sulfur speciation and destabilized Au-S complexes. The combined effect was progressively destabilizing $Au(HS)_2^-$ and ultimately triggering gold precipitation in the Dongga Au deposit. Similar Au precipitation mechanisms have been reported in other magmatic–hydrothermal systems, including the Baolun gold deposit [96] and the Baogutu gold deposit [97].

Based on previous studies of the Dongga Au deposit and the Xiongcun No.2 porphyry Cu-Au orebody [14,16,41,43], combined with the new results in this study, we further refine the genetic model of the Dongga Au deposit (Figure 14): as the mineralizing fluids continued to migrate outward into the fissure network at the periphery of the porphyry intrusion, mixing with meteoric water occurred, leading to the precipitation of early quartz–sulfide veins and Py1, which represents the initial stage of mineralization in the Dongga Au deposit (Figure 14b,f). With progressive mixing between hydrothermal fluids and meteoric water, the ore-forming condition experienced a decrease in temperature and sulfur fugacity, resulting in the co-precipitation of Py2 and associated intermediate-temperature minerals such as sphalerite. In addition, the concurrent reduction in sulfur fugacity, oxygen fugacity and temperature further decreased the activity of HS^- in the fluid, thereby destabilizing $Au(HS)_2^-$ complexes. The decoupling of $Au(HS)_2^-$ triggered gold precipitation, forming the main gold mineralization stage (Stage B1) at the Dongga Au deposit (Figure 14c,g). Subsequent evolution of the mineralizing fluid led to the precipitation of late-stage pyrrhotite, magnetite, and pyrite during late Stage B and Stage C, followed by the formation of actinolite veins (AVs) and late quartz veins (LQVs), marking the waning stage of mineralization (Figure 14e,h,i).

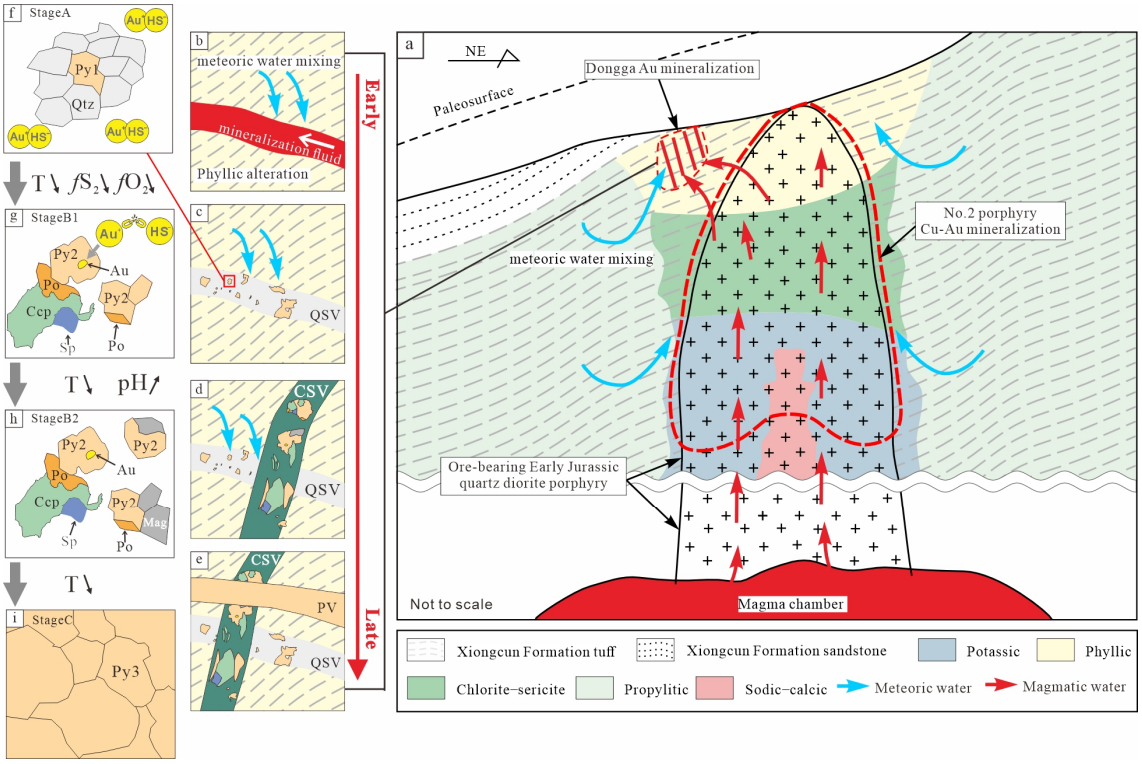


Figure 14. Schematic genetic model of the Dongga Au deposit. (**a**) Cross-sections showing the model for the Dongga gold deposit formation and the genetic relationship between the Dongga Au deposit and the No. 2 deposit in the Xiongcun ore district [16]. (**b**) The early-stage ore-forming fluids migrated into the fissure network surrounding the porphyry intrusion, leading to the formation of the phyllic alteration zone. (**c**,**f**) With the mixing of meteoric water, Py1 precipitated in QSVs during Stage A. (**d**,**g**,**h**) Progressive meteoric water influx during Stage B induced a decrease in the temperature and sulfur fugacity, triggering the precipitation of gold, chalcopyrite, sphalerite, pyrrhotite and magnetite in CSVs. (**e**,**i**) Continued cooling during Stage C contributed to the precipitation of Py3 in PVs. Py, pyrite; Po, pyrrhotite; Ccp, chalcopyrite; Sp, sphalerite; Mag, magnetite; Qtz, quartz.

7. Conclusions

(1) Elements such as Co, Ni, As, and Au are primarily incorporated into the pyrite lattice in the form of isomorphism. In contrast, Ag, Pb, Bi, Cu, and Zn predominantly occur as micro/nano-scale mineral inclusions within pyrite.

(2) Pyrite trace element systematics indicate that mineralization in the Dongga deposit occurred over a temperature range of ~400 to 270 °C, with the principal gold precipitation stage (Stage B) centered at ~340 °C. The ore-forming process was characterized by progressive cooling and significant meteoric water input, accompanied by decreases in sulfur fugacity and oxygen fugacity, as well as a shift toward higher pH conditions.

(3) Gold in the Dongga Au deposit was most likely transported in hydrothermal fluids as $Au(HS)_2^-$ complexes. Gold precipitation was driven by fluid mixing with meteoric water, which induced coupled decreases in temperature, sulfur fugacity, and oxygen fugacity. These changes reduced the availability of HS^- ligands required to stabilize $Au(HS)_2^-$, leading to the destabilization of Au–S complexes and ultimately triggering gold deposition.

Supplementary Materials: The following supporting information can be downloaded at: https://www.mdpi.com/article/10.3390/min16050539/s1, Table S1. LA-ICP-MS analyses of various pyrite generations from the Dongga Au deposit. Table S2. MASS-1.

Author Contributions: Conceptualization, H.Z. and Q.H.; methodology, H.Z. and Y.D.; formal analysis, H.Z. and Q.H.; investigation, H.Z., C.L., Z.X. and C.W.; project administration, Y.D.; validation, C.W. and K.J.; visualization, H.Z. and Y.D.; writing—original draft, H.Z.; writing—review and editing, Y.D.; funding acquisition, X.L. and K.J. All authors have read and agreed to the published version of the manuscript.

Funding: This research was funded by the Science and Technology Projects of Xizang Autonomous Region, China (XZ202601ZD000701) and Central Government Guided Local Scientific and Technological Development Funding Project (XZ202401YD0006).

Data Availability Statement: The authors confirm that the data supporting the findings of this study are available within the article.

Acknowledgments: We are grateful for the insightful suggestions from the anonymous reviewers, which greatly improved our manuscript. We appreciate Tibet Tianyuan Mineral Exploration Co., Ltd. for their support during field investigations and sampling.

Conflicts of Interest: The authors declare no conflicts of interest. Author Qing He was employed by the Western Mining Group Co., Ltd. and author Kai Jiang was employed by the Tibet Tianyuan Mineral Exploration Co., Ltd. The remaining authors declare that the research was conducted in the absence of any commercial or financial relationships that could be construed as a potential conflict of interest.

References

1. Hedenquist, J.W.; Arribas, A.; Reynolds, T.J. Evolution of an intrusion-centered hydrothermal system: Far Southeast-Lepanto porphyry and epithermal Cu-Au deposits, Philippines. *Econ. Geol.* **1998**, *93*, 373–404. [CrossRef]
2. Sillitoe, R.H. Porphyry copper systems. *Econ. Geol.* **2010**, *105*, 3–41. [CrossRef]
3. LeFort, D.; Hanley, J.; Guillong, M. Subepithermal Au-Pd mineralization associated with an alkalic porphyry Cu-Au deposit, Mount Milligan, Quesnel Terrane, British Columbia, Canada. *Econ. Geol.* **2011**, *106*, 781–808. [CrossRef]
4. Zhang, H.; Zhai, D.; Liu, J.; Li, P.L.; Li, K.; Sun, H.J. Fluid inclusion and stable (H-O-C) isotope studies of the giant Shuangjianzishan epithermal Ag-Pb-Zn deposit, Inner Mongolia, NE China. *Ore Geol. Rev.* **2019**, *115*, 103170. [CrossRef]
5. Large, R.R.; Danyushevsky, L.; Hollit, C.; Maslennikov, V.; Meffre, S.; Gilbert, S.; Bull, S.; Scott, R.; Emsbo, P.; Thomas, H.; et al. Gold and trace element zonation in pyrite using a laser imaging technique: Implications for the timing of gold in orogenic and Carlin-style sediment-hosted deposits. *Econ. Geol.* **2009**, *104*, 635–668. [CrossRef]
6. Koglin, N.; Frimmel, H.E.; Minter, W.E.L.; Brätz, H. Trace-element characteristics of different pyrite types in Mesoarchaean to Palaeoproterozoic placer deposits. *Miner. Depos.* **2010**, *45*, 259–280. [CrossRef]
7. Agangi, A.; Hofmann, A.; Wohlgemuth-Ueberwasser, C.C. Pyrite zoning as a record of mineralization in the Ventersdorp Contact Reef, Witwatersrand Basin, South Africa. *Econ. Geol.* **2013**, *108*, 1243–1272. [CrossRef]
8. Deditius, A.P.; Reich, M.; Kesler, S.E.; Utsunomiya, S.; Chryssoulis, S.L.; Walshe, J.; Ewing, R.C. The coupled geochemistry of Au and As in pyrite from hydrothermal ore deposits. *Geochim. Cosmochim. Acta* **2014**, *140*, 644–670. [CrossRef]
9. Kouhestani, H.; Ghaderi, M.; Large, R.R.; Zaw, K. Texture and chemistry of pyrite at Chah Zard epithermal gold–silver deposit, Iran. *Ore Geol. Rev.* **2017**, *84*, 80–101. [CrossRef]
10. Keith, M.; Smith, D.J.; Jenkin, G.R.T.; Holwell, D.A.; Dye, M.D. A review of Te and Se systematics in hydrothermal pyrite from precious metal deposits: Insights into ore-forming processes. *Ore Geol. Rev.* **2018**, *96*, 269–282. [CrossRef]
11. Keith, M.; Häckel, F.; Haase, K.M.; Schwarz-Schampera, U.; Klemd, R. Trace elements systematics of pyrite from submarine hydrothermal vents. *Ore Geol. Rev.* **2016**, *72*, 728–745. [CrossRef]
12. Lang, X.H.; Deng, Y.L.; Klemd, R.; Wang, X.H.; Tang, J.X. Polymetallic veins-a possible bridge between porphyry and intermediate-sulfidation deposits: A case study from Xiongcun ore district, Tibet, China. *GSA Bull.* **2026**, *138*, 1487–1508. [CrossRef]
13. Guan, H.Z.; Luosang, J.C.; Gao, L.T.; Xie, F.W. Pyrite trace-element signatures of porphyry-epithermal systems in Xizang: Implications for metallogenic discrimination and hydrothermal evolution. *Minerals* **2025**, *15*, 1113. [CrossRef]
14. Lang, X.H.; Tang, J.X.; Li, Z.J.; Huang, Y.; Ding, F.; Yang, H.H.; Xie, F.W.; Li, Z.; Wang, Q.; Zhou, Y. U-Pb and Re-Os geochronological evidence for the Jurassic porphyry metallogenic event of the Xiongcun district in the Gangdese porphyry copper belt, southern Tibet, PRC. *J. Asian Earth Sci.* **2014**, *79*, 608–622. [CrossRef]
15. Tang, J.X.; Lang, X.H.; Xie, F.W.; Gao, Y.M.; Li, Z.J.; Huang, Y.; Ding, F.; Yang, H.H.; Zhang, L.; Wang, Q.; et al. Geological characteristics and genesis of the Jurassic No. I porphyry Cu-Au deposit in the Xiongcun district, Gangdese porphyry copper belt, Tibet. *Ore Geol. Rev.* **2015**, *70*, 438–456. [CrossRef]

16. Lang, X.H.; Deng, Y.L.; He, Q.; Wang, X.H.; Harris, C.; Zhan, H.Y.; Wu, W.Z.; Wu, C.Y.; Jiang, K. Origin of the Dongga Au deposit in the giant Xiongcun porphyry Cu-Au district, Tibet, China: Constraints from multiple isotopes (Re, Os, He, Ar, H, O, S, Pb) and fluid inclusions. *Ore Geol. Rev.* **2024**, *171*, 106173. [CrossRef]
17. Yin, A.; Harrison, T.M. Geologic evolution of the Himalayan-Tibetan orogen. *Annu. Rev. Earth Planet. Sci.* **2000**, *28*, 211–280. [CrossRef]
18. DeCelles, P.G.; Kapp, P.; Gehrels, G.E.; Ding, L. Paleocene-Eocene foreland basin evolution in the Himalaya of southern Tibet and Nepal: Implications for the age of initial India-Asia collision. *Tectonics* **2014**, *33*, 824–849. [CrossRef]
19. Hu, X.M.; Garzanti, E.; Wang, J.G.; Huang, W.T.; An, W.; Webb, A. The timing of India-Asia collision onset—Facts, theories, controversies. *Earth-Sci. Rev.* **2016**, *160*, 264–299. [CrossRef]
20. An, W.; Hu, X.M.; Garzanti, E.; Wang, J.G.; Liu, Q. New precise dating of the India-Asia collision in the Tibetan Himalaya at 61 Ma. *Geophys. Res. Lett.* **2021**, *48*, e2020GL090641. [CrossRef]
21. Ding, L.; Kapp, P.; Cai, F.L.; Garzione, C.N.; Xiong, Z.Y.; Wang, H.Q.; Wang, C. Timing and mechanisms of Tibetan Plateau uplift. *Nat. Rev. Earth Environ.* **2022**, *3*, 652–667. [CrossRef]
22. Zhu, D.C.; Zhao, Z.D.; Niu, Y.L.; Mo, X.X.; Chung, S.L.; Hou, Z.Q.; Wang, L.Q.; Wu, F.Y. The Lhasa Terrane: Record of a microcontinent and its histories of drift and growth. *Earth Planet. Sci. Lett.* **2011**, *301*, 241–255. [CrossRef]
23. Bian, W.W.; Wang, S.; Yao, Y.; Jiao, X.W.; Peng, W.X.; Yang, T.S.; Zhang, S.H.; Wu, H.C.; Li, H.Y.; Deng, C.L. Location and shape of the Lhasa terrane prior to India-Asia collision. *GSA Bull.* **2023**, *135*, 2255–2274. [CrossRef]
24. Lai, W.; Hu, X.M.; Garzanti, E.; Xu, Y.; Ma, A.; Li, W. Early Cretaceous sedimentary evolution of the northern Lhasa terrane and the timing of initial Lhasa-Qiangtang collision. *Gondwana Res.* **2019**, *73*, 136–152. [CrossRef]
25. Sui, Q.L.; Wang, Q.; Zhu, D.C.; Zhao, Z.D.; Chen, Y.; Santosh, M.; Hu, Z.C.; Yuan, H.L.; Mo, X.X. Compositional diversity of ca. 110 Ma magmatism in the northern Lhasa Terrane, Tibet: Implications for the magmatic origin and crustal growth in a continent–continent collision zone. *Lithos* **2013**, *168*, 144–159. [CrossRef]
26. Allégre, C.J.; Courtillot, V.; Tapponnier, P.; Hirn, A.; Mattauer, M.; Coulon, C.; Jaeger, J.J.; Achache, J.; Schärer, U.; Marcoux, J.; et al. Structure and evolution of the Himalaya-Tibet orogenic belt. *Nature* **1984**, *307*, 17–22. [CrossRef]
27. Hou, Z.Q.; Duan, L.F.; Lu, Y.J.; Zheng, Y.C.; Zhu, D.C.; Yang, Z.M.; Yang, Z.S.; Wang, B.D.; Pei, Y.R.; Zhao, Z.D.; et al. Lithospheric architecture of the Lhasa Terrane and its control on ore deposits in the Himalayan-Tibetan orogen. *Econ. Geol.* **2015**, *110*, 1541–1575. [CrossRef]
28. Zhu, D.C.; Mo, X.X.; Niu, Y.; Zhao, Z.D.; Wang, L.Q.; Liu, Y.S.; Wu, F.Y. Geochemical investigation of Early Cretaceous igneous rocks along an east–west traverse throughout the central Lhasa Terrane, Tibet. *Chem. Geol.* **2009**, *268*, 298–312. [CrossRef]
29. Cao, M.J.; Qin, K.Z.; Li, G.M.; Li, J.X.; Zhao, J.X.; Evans, N.J.; Hollings, P. Tectono-magmatic evolution of Late Jurassic to Early Cretaceous granitoids in the west central Lhasa subterrane, Tibet. *Gondwana Res.* **2016**, *39*, 386–400. [CrossRef]
30. Zhu, D.C.; Mo, X.X.; Niu, Y.; Zhao, Z.D.; Wang, L.Q.; Pan, G.T.; Wu, F.Y. Zircon U–Pb dating and in-situ Hf isotopic analysis of Permian peraluminous granite in the Lhasa terrane, southern Tibet: Implications for Permian collisional orogeny and paleogeography. *Tectonophysics* **2009**, *469*, 48–60. [CrossRef]
31. Wang, X.H.; Lang, X.H.; Klemd, R.; Deng, Y.L.; Tang, J.X. Subduction initiation of the Neo-Tethys oceanic lithosphere by collision-induced subduction transference. *Gondwana Res.* **2022**, *104*, 54–69. [CrossRef]
32. Dong, X.; Zhang, Z.M.; Niu, Y.L.; Tian, Z.L.; Zhang, L.L. Reworked Precambrian metamorphic basement of the Lhasa terrane, southern Tibet: Zircon/titanite U-Pb geochronology, Hf isotope and geochemistry. *Precambrian Res.* **2020**, *336*, 105496. [CrossRef]
33. Mo, X.X.; Hou, Z.; Niu, Y.L.; Dong, G.; Qu, X.; Zhao, Z.; Yang, Z. Mantle contributions to crustal thickening in south Tibet in response to the India–Asia collision. *Lithos* **2007**, *96*, 225–242. [CrossRef]
34. Zhu, D.C.; Wang, Q.; Chung, S.L.; Cawood, P.A.; Zhao, Z.D. Gangdese magmatism in southern Tibet and India–Asia convergence since 120 Ma. *Geol. Soc. Lond. Spec. Publ.* **2019**, *483*, 583–604. [CrossRef]
35. Ji, W.Q.; Wu, F.Y.; Chung, S.L.; Li, J.X.; Liu, C.Z. Zircon U-Pb geochronology and Hf isotopic constraints on petrogenesis of the Gangdese batholith, southern Tibet. *Chem. Geol.* **2009**, *262*, 229–245. [CrossRef]
36. Ji, W.Q.; Wu, F.Y.; Liu, C.Z.; Chung, S.L. Early Eocene crustal thickening in southern Tibet: New age and geochemical constraints from the Gangdese batholith. *J. Asian Earth Sci.* **2012**, *53*, 82–95. [CrossRef]
37. Deng, Y.L.; Lang, X.H.; Wang, X.H.; Santosh, M.; He, Q.; Yin, Q. Early Mesozoic arc-back-arc system in the leading edge of the Tibetan Plateau. *Lithos* **2021**, *406*, 106530. [CrossRef]
38. Liu, A.L.; Wang, Q.; Zhu, D.C.; Cawood, P.A.; Xia, Y.; Li, S.M.; Liu, S.A.; Huang, F.; Liu, L.; Zhao, Z.D.; et al. Temporal and spatial variations of enriched source components in Linzizong volcanic succession, Tibet, and implications for the India-Asia collision. *J. Petrol.* **2022**, *63*, egab103. [CrossRef]
39. Lang, X.; Tang, J.; Yin, Q.; Cui, Z.; Huang, Y.; Zhang, J.; Gao, Y.; Li, Z.; Ding, F.; Xie, F.; et al. Geochemistry and genesis of Eocene lamprophyres in the Xiongcun porphyry copper-gold district, southern margin of the Lhasa terrane, Tibet, China. *Geochem. J.* **2017**, *51*, 123–142. [CrossRef]

40. Xie, F.W.; Tang, J.X.; Chen, Y.; Lang, X.H. Apatite and zircon geochemistry of Jurassic porphyries in the Xiongcun district, southern Gangdese porphyry copper belt: Implications for petrogenesis and mineralization. *Ore Geol. Rev.* **2018**, *96*, 98–114. [CrossRef]
41. Lang, X.H.; Wang, X.H.; Deng, Y.L.; Tang, J.X.; Xie, F.W.; Yang, Z.Y.; Yin, Q.; Jiang, K. Hydrothermal evolution and ore precipitation of the No. 2 porphyry Cu-Au deposit in the Xiongcun district, Tibet: Evidence from cathodoluminescence, fluid inclusions, and isotopes. *Ore Geol. Rev.* **2019**, *114*, 103141. [CrossRef]
42. Lang, X.H.; Wang, X.H.; Deng, Y.L.; Tang, J.X.; Xie, F.W.; Zou, Y.; Huang, Y.; Li, Z.; Yin, Q.; Jiang, K. Early Jurassic volcanic rocks in the Xiongcun district, southern Lhasa subterrane, Tibet: Implications for the tectono-magmatic events associated with the early evolution of the Neo-Tethys Ocean. *Lithos* **2019**, *340–341*, 166–180. [CrossRef]
43. Yin, Q.; Lang, X.H.; Cui, Z.W.; Yan, Z.Y.; Xie, F.W.; Wang, X.H. Geology and geochemistry constraints on the genesis of the No. 2 porphyry copper-gold deposit in the Xiongcun district, Gangdese porphyry copper belt, Tibet, China. *Appl. Ecol. Environ. Res.* **2017**, *15*, 477–508. [CrossRef]
44. Chen, X.; Zheng, Y.Y.; Gao, S.B.; Wu, S.; Jiang, X.J.; Jiang, J.S.; Cai, P.J.; Lin, C.G. Ages and petrogenesis of the Late Triassic andesitic rocks at the Luerma porphyry Cu deposit, western Gangdese, and implications for regional metallogeny. *Gondwana Res.* **2020**, *85*, 103–123. [CrossRef]
45. Sun, X.; Lu, Y.J.; Li, Q.; Li, R.Y. A downgoing Indian lithosphere control on along-strike variability of porphyry mineralization in the Gangdese belt of southern Tibet. *Econ. Geol.* **2021**, *116*, 29–46. [CrossRef]
46. Xue, Q.Q.; Zhang, L.P.; Chen, S.; Guo, K.; Li, T.; Han, Z.; Sun, W.D. Tracing black shales in the source of a porphyry Mo deposit using molybdenum isotopes. *Geology* **2023**, *51*, 688–692. [CrossRef]
47. Lin, B.; Tang, J.X.; Tang, P.; Beaudoin, G.; Laflamme, C.; Li, F.Q.; Zheng, W.B.; Song, Y.; Qi, J.; Sun, M.; et al. Multipulsed magmatism and duration of hydrothermal system of the giant Jiama porphyry Cu system, Tibet, China. *Econ. Geol.* **2024**, *119*, 201–217. [CrossRef]
48. Zhang, L.Q.; Chen, X.L.; Zou, S.H.; Xu, D.R.; Wang, X.N.; Wang, H. Petrogenesis, oxidation state and volatile content of Dongga tonalite in the Gangdese belt, Xizang: Implication for porphyry Cu mineralization. *Acta Geochim.* **2024**, *43*, 280–295. [CrossRef]
49. Tang, J.X.; Li, Z.J.; Lang, X.H. Minerals exploration report in the Xiongcun district: Xietongmen County, Tibet. In *Private Report*; Tibet Tianyuan Minerals Exploration Ltd.: Beijing, China, 2012; p. 341. (In Chinese)
50. Tafti, R.; Lang, J.R.; Mortensen, J.K.; Oliver, J.L.; Rebagliati, C.M. Geology and geochronology of the Xietongmen (Xiongcun) Cu-Au porphyry district, southern Tibet, China. *Econ. Geol.* **2014**, *109*, 1967–2001. [CrossRef]
51. Lang, X.H.; Guo, W.B.; Wang, X.H.; Deng, Y.L.; Yang, Z.Y.; Xie, F.W.; Li, Z.; Zhang, Z.; Jiang, K. Petrogenesis and tectonic implications of the ore-bearing porphyries in the Xiongcun district: Constraints from the geochronology and geochemistry. *Acta Petrol. Sin.* **2019**, *35*, 2105–2123, (In Chinese with English abstract).
52. Wang, X.; Lang, X.; Tang, J.; Deng, Y.; He, Q.; Xie, F.; Li, L.; Yin, Q.; Li, Z.J.; Li, Z.; et al. Early Carboniferous back-arc rifting-related magmatism in southern Tibet: Implications for the history of the Lhasa terrane separation from Gondwana. *Tectonics* **2020**, *39*, e2020TC006237. [CrossRef]
53. Lang, X.H.; Wang, X.H.; Tang, J.X.; Deng, Y.L.; Cui, Z.W.; Yin, Q.; Xie, F.W. Composition and age of Jurassic diabase dikes in the Xiongcun porphyry copper-gold district, southern margin of the Lhasa terrane, Tibet, China: Petrogenesis and tectonic setting. *Geol. J.* **2018**, *53*, 1973–1993. [CrossRef]
54. Lang, X.H.; Deng, Y.L.; Wang, X.H.; Tang, J.X.; Xie, F.W.; Yang, Z.Y.; Yin, Q.; Jiang, K. Reduced fluids in porphyry copper-gold systems reflect the occurrence of the wall-rock thermogenic process: An example from the No. 1 deposit in the Xiongcun district, Tibet, China. *Ore Geol. Rev.* **2020**, *118*, 103212. [CrossRef]
55. Su, D.K.; Huang, W. *Geological Survey Report of Donggapu Gold and Copper Mine, Rongma Township, Xietongmen County, Tibet Autonomous Region*; The Sixth Geological Brigade of the Department of Geology and Mineral Resources of Tibet Autonomous Region: Lhasa, China, 2003. (In Chinese)
56. Zong, K.Q.; Klemd, R.; Yuan, Y.; He, Z.Y.; Guo, J.L.; Shi, X.L.; Liu, Y.S.; Hu, Z.C.; Zhang, Z.M. The assembly of Rodinia: The correlation of early Neoproterozoic (ca. 900 Ma) high-grade metamorphism and continental arc formation in the southern Beishan Orogen, southern Central Asian Orogenic Belt (CAOB). *Precambrian Res.* **2017**, *290*, 32–48. [CrossRef]
57. Hu, Z.C.; Zhang, W.; Liu, Y.S.; Gao, S.; Li, M.; Zong, K.Q.; Chen, H.H.; Hu, S.H. "Wave" signal-smoothing and mercury-removing device for laser ablation quadrupole and multiple collector ICPMS analysis: Application to lead isotope analysis. *Anal. Chem.* **2015**, *87*, 1152–1157. [CrossRef]
58. Liu, Y.S.; Hu, Z.C.; Gao, S.; Günther, D.; Xu, J.; Gao, C.G.; Chen, H.H. In situ analysis of major and trace elements of anhydrous minerals by LA-ICP-MS without applying an internal standard. *Chem. Geol.* **2008**, *257*, 34–43. [CrossRef]
59. Reich, M.; Kesler, S.E.; Utsunomiya, S.; Palenik, C.S.; Chryssoulis, S.L.; Ewing, R.C. Solubility of gold in arsenian pyrite. *Geochim. Cosmochim. Acta* **2005**, *69*, 2781–2796. [CrossRef]
60. Román, N.; Reich, M.; Leisen, M.; Morata, D.; Barra, F.; Deditius, A.P. Geochemical and micro-textural fingerprints of boiling in pyrite. *Geochim. Cosmochim. Acta* **2019**, *264*, 60–85. [CrossRef]

61. Cook, N.; Ciobanu, C.; George, L.; Zhu, Z.Y.; Wade, B.; Ehrig, K. Trace element analysis of minerals in magmatic-hydrothermal ores by laser ablation inductively coupled plasma mass spectrometry: Approaches and opportunities. *Minerals* **2016**, *6*, 111. [CrossRef]
62. Fleet, M.E.; Chryssoulis, S.L.; MacLean, P.J.; Davidson, R.; Weisener, C.G. Arsenian pyrite from gold deposits; Au and As distribution investigated by SIMS and EMP, and color staining and surface oxidation by XPS and LIMS. *Can. Mineral.* **1993**, *31*, 1–17. Available online: https://www.researchgate.net/publication/279553357_Arsenian_pyrite_from_gold_deposits_Au_and_As_distribution_investigated_by_SIMS_and_EMP_and_color_staining_and_surface_oxidation_by_XPS_and_LIMS (accessed on 1 May 2026).
63. Pokrovski, G.S.; Kokh, M.A.; Proux, O.; Hazemann, J.L.; Bazarkina, E.F.; Testemale, D.; Escoda, C.; Boiron, M.C.; Blanchard, M.; Aigouy, T.; et al. The nature and partitioning of invisible gold in the pyrite-fluid system. *Ore Geol. Rev.* **2019**, *109*, 545–563. [CrossRef]
64. Zhang, H.; Cai, Y.F.; Sha, G.; Brugger, J.; Pring, A.; Ni, P.; Qian, G.J.; Luo, Z.J.; Zhang, Y.; Tan, W. Effects of arsenic on the distribution and mode of occurrence of gold during fluid-pyrite interaction: A case study of pyrite from the Qiucun gold deposit, China. *Am. Mineral.* **2022**, *107*, 914–929. [CrossRef]
65. Shannon, R.D. Revised effective ionic radii and systematic studies of interatomic distances in halides and chalcogenides. *Found. Crystallogr.* **1976**, *32*, 751–767. [CrossRef]
66. Morse, J.W.; Luther, G.W. Chemical influences on trace metal-sulfide interactions in anoxic sediments. *Geochim. Cosmochim. Acta* **1999**, *63*, 3373–3378. [CrossRef]
67. Zhao, H.X.; Frimmel, H.E.; Jiang, S.Y.; Dai, B.Z. LA-ICP-MS trace element analysis of pyrite from the Xiaoqinling gold district, China: Implications for ore genesis. *Ore Geol. Rev.* **2011**, *43*, 142–153. [CrossRef]
68. Revan, M.K.; Genç, Y.; Maslennikov, V.V.; Maslennikov, S.P.; Large, R.R.; Danyushevsky, L.V. Mineralogy and trace-element geochemistry of sulfide minerals in hydrothermal chimneys from the Upper-Cretaceous VMS deposits of the Eastern Pontide orogenic belt (NE Turkey). *Ore Geol. Rev.* **2014**, *63*, 129–149. [CrossRef]
69. Bezmen, N.I.; Tikhomirova, V.I. Effect of temperature on cobalt and nickel distribution between iron sulfides and solutions of different composition. *Geokhimiya* **1975**, *11*, 1691–1697. (In Russian)
70. Einaudi, M.T.; Hedenquist, J.W.; Inan, E.E. Sulfidation state of fluids in active and extinct hydrothermal systems: Transitions from porphyry to epithermal environments. In *Volcanic, Geothermal, and Ore-Forming Fluids: Rulers and Witnesses of Processes within the Earth*; Simmons, S.F., Graham, I., Eds.; Society of Economic Geologists: Littleton, CO, USA, 2003; Volume 10, pp. 285–313.
71. Charles, R.W.; Janecky, D.R.; Goff, F.; McKibben, M.A. Chemographic and thermodynamic analysis of the paragenesis of the major phases in the vicinity of the 6120-foot (1866 m) flow zone, California State Well 2–14. *J. Geophys. Res.* **1988**, *93*, 13145–13157. [CrossRef]
72. Baumgartner, R.; Fontboté, L.; Vennemann, T. Mineral zoning and geochemistry of epithermal polymetallic Zn-Pb-Ag-Cu-Bi mineralization at Cerro de Pasco, Peru. *Econ. Geol.* **2008**, *103*, 493–537. [CrossRef]
73. Peng, Z.; Watanabe, M.; Hoshino, K.; Sueoka, S.; Yano, T.; Nishido, H. The Machangqing copper-molybdenum deposits, Yunnan, China—An example of Himalayan porphyry-hosted Cu-Mo mineralization. *Miner. Petrol.* **1998**, *63*, 95–117. [CrossRef]
74. Palyanova, G. Gold fineness and Au/Ag ratios of pyrite-containing ores as additional indicators of physico-chemical conditions of hydrothermal ore formation. *J. Geochem. Explor.* **2009**, *101*, 79. [CrossRef]
75. Phillips, N. *Formation of Gold Deposits*; Springer Press: Berlin/Heidelberg, Germany, 2022; pp. 254–274.
76. Kouzmanov, K.; Pokrovski, G.S. Hydrothermal controls on metal distribution in porphyry Cu (-Mo-Au) systems. *Soc. Econ. Geol. Spec. Publ.* **2012**, *16*, 573–618. [CrossRef]
77. Miao, Y.; Zhou, Y.; Li, W.C.; Romer, R.L.; Zjpi, X.J.; Li, C.; Chen, M.S. Episodic ore redistribution in Carlin-type gold deposits in southeastern Yunnan Province, SW China. *Econ. Geol.* **2026**, *121*, 219–239. [CrossRef]
78. Peng, H.W.; Fan, H.R.; Lecumberri-Sanchez, P.; Lai, J.Q.; Hu, H.L.; Lan, T.G.; Li, X.H. Fluid evolution and ore genesis of the Tiantangshan granite-related vein-type Rb-Sn-W deposit, south China: Constraints from LA-ICP-MS analyses of fluid inclusions. *Miner. Depos.* **2023**, *58*, 751–769. [CrossRef]
79. Xiao, J.D.; Xie, Z.J.; Xia, Y.; Lan, T.G.; Zhang, L.; Pan, L.C.; Hu, H.L.; Wang, H.; Tan, Q.P.; Xu, Y. Predominant fracture gold in the Jiaodong gold province, China: Constraints on gold mineralization processes. *Ore Geol. Rev.* **2024**, *165*, 105915. [CrossRef]
80. Wilkinson, J.J. Fluid inclusions in hydrothermal ore deposits. *Lithos* **2001**, *55*, 229–272. [CrossRef]
81. Nejadhadad, M.; Taghipour, B.; Lentz, D.R. Implications of multiple fluids in the deposition of Pb-Zn-Ba deposits in the Alvand Mountain, Golpayegan, Iran: Evidence from fluid inclusions and O, C, S isotopes. *Ore Geol. Rev.* **2023**, *153*, 105300. [CrossRef]
82. Niu, P.P.; Muñoz, M.; Mathon, O.; Xiong, S.F.; Jiang, S.Y. Mechanism of germanium enrichment in the world-class Huize MVT Pb–Zn deposit, southwestern China. *Miner. Depos.* **2024**, *59*, 995–1016. [CrossRef]
83. Rainoldi, A.L.; Beaufort, D.; Franchini, M.B.; Giusiano, A.; Petit, S.; Patrier, P.; Pons, M.J. Vanadium mineralization at Los Chihuidos sediment-hosted Cu–V deposit, Neuquén Basin, Argentina: An approach to vanadium ore forming processes. *Geosci. Front.* **2024**, *15*, 101724. [CrossRef]

84. Shi, J.P.; Wu, G.; Chen, G.Z.; Yang, F.; Zhang, T.; Jiang, B.; Liu, W. Genesis of the supergiant Shuangjianzishan Ag–Pb–Zn deposit in the southern Great Xing'an Range, NE China: Constraints from geochronology, isotope geochemistry, and fluid inclusion. *Minerals* **2024**, *14*, 60. [CrossRef]
85. Williams-Jones, A.E.; Bowell, R.J.; Migdisov, A.A. Gold in solution. *Elements* **2009**, *5*, 281–287. [CrossRef]
86. Zhai, D.G.; Liu, J.J.; Cook, N.J.; Wang, X.L.; Yang, Y.Q.; Zhang, A.L.; Jiao, Y.C. Mineralogical, textural, sulfur and lead isotope constraints on the origin of Ag-Pb-Zn mineralization at Bianjiadayuan, Inner Mongolia, NE China. *Miner. Depos.* **2019**, *54*, 47–66. [CrossRef]
87. Boutier, A.; Martinez, I.; Sissmann, O.; Agostini, S.; Daniel, I.; Van Baalen, M.; Mana, S.; Brovarone, A.V. Complexity of graphite formation in response to metamorphic methane generation and transformation in an orogenic ultramafic body. *Geochim. Cosmochim. Acta* **2024**, *364*, 166–183. [CrossRef]
88. Simmons, S.F.; Brown, K.L.; Tutolo, B.M. Hydrothermal transport of Ag, Au, Cu, Pb, Te, Zn, and other metals and metalloids in New Zealand geothermal systems: Spatial patterns, fluid-mineral equilibria, and implications for epithermal mineralization. *Econ. Geol.* **2016**, *111*, 589–618. [CrossRef]
89. Cook, N.J.; Ciobanu, C.L.; Mao, J. Textural control on gold distribution in As-free pyrite from the Dongping, Huangtuliang and Hougou gold deposits, North China Craton (Hebei Province, China). *Chem. Geol.* **2009**, *264*, 101–121. [CrossRef]
90. Wang, C.M.; Deng, J.; Bagas, L.; He, X.Y.; Zhang, J. Origin and classification of the Late Triassic Huaishuping gold deposit in the eastern part of the Qinling-Dabie Orogen, China: Implications for gold metallogeny. *Miner. Depos.* **2021**, *56*, 725–742. [CrossRef]
91. Sheng, Y.M.; Tang, L.; Zhang, S.T.; Santosh, M.; Hu, X.K. Influence of fluid-rock interaction on gold mineralization in the Dongwan deposit, East Qinling, China: Constraints from systematic sulfur isotope and trace element geochemistry. *Ore Geol. Rev.* **2022**, *142*, 104718. [CrossRef]
92. Falkenberg, J.J.; Keith, M.; Melfos, V.; Hohl, M.; Haase, K.M.; Voudouris, P.; Höss, A.; Wenske, J.; Klemd, R.; Beier, C.; et al. Insights into fluid evolution and Re enrichment by mineral micro-analysis and fluid inclusion constraints: Evidence from the Maronia Cu-Mo ± Re ± Au porphyry system in NE Greece. *Miner. Depos.* **2024**, *59*, 1407–1431. [CrossRef]
93. Zhu, Y.; An, F.; Tan, J. Geochemistry of hydrothermal gold deposits: A review. *Geosci. Front.* **2011**, *2*, 367–374. [CrossRef]
94. Hayashi, K.I.; Ohmoto, H. Solubility of gold in NaCl- and H2S-bearing aqueous solutions at 250–350 °C. *Geochim. Cosmochim. Acta* **1991**, *55*, 2111–2126. [CrossRef]
95. Pokrovski, G.S.; Kokh, M.A.; Guillaume, D.; Dubessy, J. Sulfur radical species form gold deposits on Earth. *Proc. Natl. Acad. Sci. USA* **2015**, *112*, 13484–13489. [CrossRef] [PubMed]
96. Yan, S.; Shan, Q.; Xu, D.R.; Yu, X.Y. Contribution of bismuth melts to gold endowment in the Baolun gold deposit, Hainan Island, South China. *Ore Geol. Rev.* **2024**, *173*, 106258. [CrossRef]
97. An, F.; Zhu, Y.F. Native antimony in the Baogutu gold deposit (west Junggar, NW China): Its occurrence and origin. *Ore Geol. Rev.* **2010**, *37*, 214–223. [CrossRef]

Disclaimer/Publisher's Note: The statements, opinions and data contained in all publications are solely those of the individual author(s) and contributor(s) and not of MDPI and/or the editor(s). MDPI and/or the editor(s) disclaim responsibility for any injury to people or property resulting from any ideas, methods, instructions or products referred to in the content.